Optomechanical Design, Analysis, and Testing of the Nanosatellite Optical Downlink Experiment

by

Derek Barnes

Submitted to the Department of Aerospace Engineering
in partial fulfillment of the requirements for the degree of

Master of Science in Aerospace Engineering

at the

MASSACHUSETTS INSTITUTE OF TECHNOLOGY

June 2018

Author ... Signature redacted .....
Department of Aerospace Engineering
June 8, 2018

Certified by .. Signature redacted .....
Kerri Cahoy
Associate Professor of Aeronautics and Astronautics
Thesis Supervisor

Accepted by ..... Signature redacted
Hamsa Balakrishnan
Associate Professor of Aeronautics and Astronautics
Chair, Graduate Program Committee

Optomechanical Design, Analysis, and Testing of the Nanosatellite Optical Downlink Experiment

by

Derek Barnes

Submitted to the Department of Aerospace Engineering
on June 8, 2018, in partial fulfillment of the
requirements for the degree of
Master of Science in Aerospace Engineering

Abstract

As space payloads are miniaturized, many companies and government agencies are fielding small satellites that can compete with traditional "monolithic" satellites. More than 250 CubeSats were launched into orbit in 2017 alone. As the density of increasingly capable small satellites in orbit increases, many CubeSat operators are finding that current radio frequency (RF) communications are not capable of transmitting the amount of data desired. Free Space Optical (FSO) communication systems offer an alternative to traditional RF systems that can offer data rates more than an order of magnitude faster than RF communication while using less power and mass.

This thesis describes the optomechanical design, analysis, and test results of the Nanosatellite Optical Downlink Experiment (NODE). NODE is a CubeSat FSO communication system demonstration mission. The NODE payload is a hosted payload that is designed to establish and maintain optical alignment, survive launch loads, and maintain allowable flight temperatures. Resonant frequency analysis predicts the first resonant frequency to be 500 Hz. Fastener analysis predicts margins of safety greater than 200 for shear, tensile, and separation analysis. Depressurization analysis is performed to calculate expected payload pressure loads and optical bond analysis is performed and predicts a margin of safety of 5 for adhesive optical bonds in a worst-case scenario. Thermal analysis predicts the NODE payload to maintain required operational and survival temperatures in worst all scenarios. Vibration testing of the payload identified the first resonant frequency of the payload to be at 500 Hz. Component level TVAC testing of the Erbium Doped Fiber Amplifier is performed and an optical loss of 0.2 dB is measured. FSM pointing repeatability testing is performed and pointing capability is verified to be within +- 3.6 arc minutes of the commanded location.

Thesis Supervisor: Kerri Cahoy
Title: Associate Professor of Aeronautics and Astronautics

Acknowledgments

I would first like to thank my advisor Kerri Cahoy. She has provided excellent guidance throughout my career as both and undergraduate and graduate student and has given me excellent opportunities to grow professionally during my time at MIT.

I would also like to thank my parents: my mother and father for supporting me throughout my undergraduate and graduate education, and Halston Taylor for encouraging me to apply to MIT as an undergrad and beleving in me before I did myself. Thank you to my teammates and friends who helped and kept me going along the way.

Contents

List of Figures

List of Tables

Chapter 1

Introduction

Small satellites are an increasingly popular platform for space missions as miniaturization of components and payloads allows smaller spacecraft to be built with capabilities that can compete with those of larger monolithic satellites. CubeSats, a standardized form factor of nanosatellites (less than 4kg and built in "1U" sections of 10 cm $\times$ 10 cm), are responsible for more than 90% of past launches. In 2017 more than 250 CubeSats were launched into orbit [21]. While CubeSats were initially intended as a tool to help universities teach space system design, commercial industry has started to use the CubeSat form factor and is now responsible for 50 percent of currently planned and launched CubeSats [21].

Traditional RF communication systems are bandwidth limited, and can achieve data-rates ranging from 10-220 Mbps [20], with proposed systems reaching into the 300 Mpbs range [43]. Additionally, RF licensing through the FCC can cost companies more than $500,000 per application [13], take years to complete, and is often denied [15]. High data rate RF communication systems require significant power usage [44], and mechanical accommodation of high gain antennas often require deployables which add mechanical complexity and risk [2].

Optical communications systems offer an alternative system that allows for data rates an order of magnitude higher than RF systems while using less power and mass [27]. Optical communication ground stations are more compact and not subject to FCC licensing which can avoid costly RF licensing and ground station usage [27] [34].

Optical communication systems must be pointed more precisely than traditional RF systems and are sensitive to misalignment in optical elements [45] [26].

Optomechanical engineering is a sub-field of optical engineering where optics are integrated into a mechanical structure and to form an instrument [18]. Optomechanical engineers must make decisions on material choice, mechanical design, optical element mounting, assembly, and alignment while maintaining optical system performance metrics. Optomechanical design requires integrated models where the optical systems performance is predicted. These models often include analysis on optical alignment, thermoelastic effects,resonant frequencies, static loading, and fastener analysis. Optomechanical engineering often includes all phases of mission development, and often includes involvement in testing and integration [18].

This thesis describes the optomechanical design, analysis, and testing of the Nanosatellite Optical Downlink Experiment (NODE).The NODE mission plans to demonstrate optical communication onboard a CubeSat [19][33][26][45][29][33][34]. NODE will use a commercial-off-the-shelf (COTS) fast steering mirror (FSM) to steer a 1550 nm downlink beam to an optical ground station on Earth [45]. NODE plans to achieve a datarate of 10-40 Mbps [6]. NODE will operate from low earth orbit (LEO) onboard a host spacecraft.

1.1 Motivation for CubeSat Optical Communications

RF licensing required by the FCC can be prohibitively expensive and time consuming for companies looking to enter into the small satelite industry [13] and can be more expensive than launch costs [40]. Recent proposed regulation changes by the FCC aim to reduce licensing costs to $30,000 per application, but the reduced licensing cost only applies to small groups of satellites in quickly decaying orbits [13]. While some companies can afford to pay licensing costs and are granted licenses [12], other companies are denied licensing and can be subject to enforcement action [15]. Optical communication systems are less likely to interfere with eachother and are are not currently regulated by the FCC [33].

NASA believes that optical communication systems can offer data rates up to 20 times higher, can use up to 50% less mass, and can have a 65% savings in power when compared to traditional RF communications [27]. The NASA Lunar Laser Communication Demonstration (LLCD) misssion has demonstrated a data rate of 622 mbps from the Moon to the Earth, and smaller spacecraft have demonstrated optical links between to and from the Earth and other spacecraft, but none have demonstrated an orbital optical communication system for the CubeSat form factor [28] [8][35]. Aerospace Corporation recently launched AeroCube-7a with the goal of demonstrating CubeSat lasercom, but as of December 2017 has yet to close a link [35].

1.2 Existing Optical Communication Systems

Optical communication systems have already demonstrated their capabilities for secure high data rate communications onboard space based platforms. In 1994 the Japanese Space Agency (JAXA) launched the ETS-VI satellite carrying the Laser Communication Exeriment (LCE) [19]. The instrument was able to demonstrate a 1 Mbps bidirectional link[19]. In 2001 by the European Space Agency (ESA) launched the geostationary satellite ARTEMIS [39] and the USA launched GeoLITE developed by Lincoln labs in Lexington Massachusetts [22]. Both ARTEMIS and GeoLITE carried optical communication payloads, ARTEMIS was able to achieve a data rate of 50 Mbps and while GeoLITE is recognized as a successful demonstration not published data is available on the system [22]. The ESA later developed an optical communication payload for the EDRS system, where they demonstrated optical communication crosslinks between a geostationary satellite and low earth orbit (LEO) satellite [32]. In 2008 the US satellite NFIRE and German Aerospace Center (DLR) satellite TerraSAR-X demonstrated an optical crosslink between two satellites [36]. In 2013 MIT Lincoln Laboratory successfully tested the Lunar Laser Communication Demonstration (LLCD) and was able to achieve a 622 Mbps downlink from the Moon to the Earth[28].

Optical communication platforms have also been demonstrated in LEO. In 2005 the Japanese Optical Inter-orbit Communication Engineering Test Satellite (OICETS) was launched to LEO carrying the Laser Utilizing Communications Equipment (LUCE) instrument which was able to demonstrate inter-satellite crosslinks between ARTEMIS and OICETS. In 2014 the NASA Jet Propulsion Laboratory developed the Optical Payload for Lasercom Science (OPALS) which was mounted to the International Space Station.

Many different organizations are currently attempting to demonstrate small satellite optical communication. The Japanese Rapid International Scientific Experiment Satellite (RISESat) carries the Very Small Optical TrAnsponder (VSOTA) which plans to demonstrate optical communication. While RISESat is much larger than a CubeSat, the VSOTA instrument is one of many hosted payloads [30]. Aerospace Corp. has designed an optical communication system that flew on AeroCube 7a, but experienced attitude determination and control errors before they could successfully test their optical communication system [8]. They relaunched two replacements (AeroCube 7b and 7c) in December 2017, but have yet to demonstrate the optical communication system as of December 2017 [35]. The commercial company Sinclair Interplanetary (Located in Toronto Canada) is currently developing an optical communication system for CubeSats but has yet to test the system on-orbit[17].

NASA is currently developing optical communication terminals for multiple missions. The Laser Communications Relay Demonstration (LCRD) developed by NASA Goddard will launch in 2019 and aims to demonstrate high rate bi-directional communication between Earth and GEO [7]. LCRD also aims to test modulation schemes developed for deep-space optical communications as well as real-time optical relay though the spacecraft from one ground station to another ground station. NASA's Psyche mission that launches in 2022 will carry the Deep Space Optical communications (DSOC) instrument and plans to demonstrate optical communication systems from the asteroid belt [14]. MIT Lincoln Laboratory have announced plans to demonstrate 200 Gbps data rates from a CubeSat in 2019 [41].

Table 1.1 compares existing and planned optical communications missions with

their respective link types, mass, and data rates while indicating whether they have successfully closed an optical communication link.

Table 1.1: Examples of Past Optical Communications Systems

Mission Name	Mass [kg]	Launch Year	Data Rate [Mbps]	Link Type	Demonstrated On-orbit?
LCE [19]	22.4	1994	1	GEO to Ground	Yes
ARTEMIS [39]	160	2001	50	GEO to Ground	Yes
GeoLITE [22][19]	-	2001	-	GEO to Ground	Yes
EDRS [32]	360	2016	600	GEO to LEO	Yes
NFIRE and TerraSAR-X [36]	494	2007	500000	GEO to LEO	Yes
LLCD	32	2013	622	Lunar Orbit to Ground	Yes
OICETS	140	2005	50	LEO to/from GEO	Yes
OPALS	50	2014	50	LEO to Ground	Yes
RISESAT	<1	2018	0.1	LEO to Ground	No
AeroCube 7a	CubeSat size	2015	5-50	LEO to/from Ground	No
AeroCube 7b/c	CubeSat size	2017	5-50	LEO to/from Ground	No
Sinclair Interplanetary Lasercom System	0.335	2017	100/1000 (cross/-down)	Component	No
TBIRD	CubeSat size	2019	200000	LEO to Ground	No

1.3 Overview of NODE Mission

The NODE mission plans to demonstrate optical communication onboard a CubeSat [19][33][26][45][29][33][34]. The mission aims to be low cost by utilizing commercial off the shelf components (COTS) to steer a 1550 nm modulated laser beam to a low-cost 1 m diameter ground station (developed by MIT Star Laboratory [34][9]). The NODE mission aims to achieve a data rate between 10-40 Mbps [6]. The NODE payload is required to be compatible with host CubeSat satellites and can tolerate host pointing error of $\pm$ 3 degrees. The NODE system is monostatic (one aperture) and contains a beacon receiver that is used for closed loop ground station tracking. The NODE payload is 96 mm $\times$ 96 mm $\times$ 119 mm. Figure 1-1 shows the dimensions of the NODE payload on the left-most side, a mechanical prototype in the middle, and the MIT developed ground station (PorteL) [34][9]. Table 1.2 summarizes technical details of the NODE transmitter.

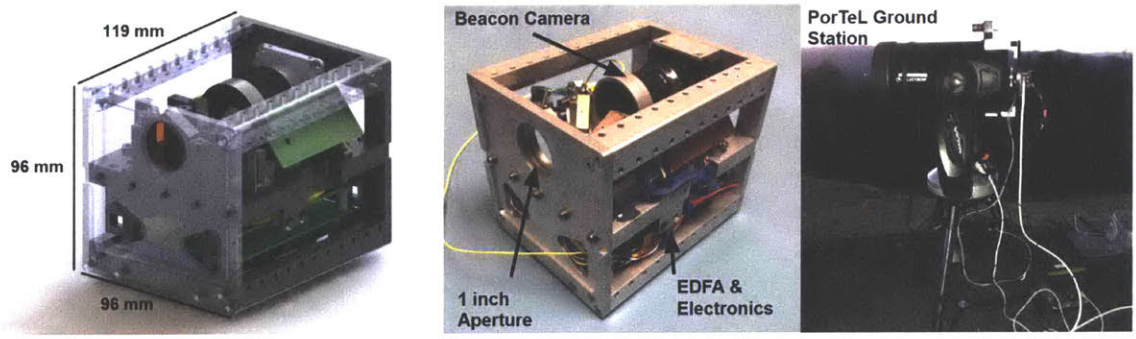

Figure 1-1: From left to right; CAD Depiction of NODE payload, Engineering Model, and ground station [34].

Figure 1-2 presents a simplified block diagram of NODE optical elements critical to the optomechanical design. The NODE system is built in a Master Oscillatory Power Amplification (MOPA) architecture in which a seed laser (Transmitter Optical Sub Assembly- TOSA) generates a laser beam, which is then modulated by a Fiber Bragg Grating (FBG) [19][26]. This modulated signal is then passed through an Erbium Doped Fiber Amplifier (EDFA) and routed to a collimator where it becomes a free-space beam. This beam hits a FSM where it is then steered out of the satellite into a ground station where the beam is received and demodulated. The system also contains

Table 1.2: Summary of NODE technical details

Application	Low-cost compact optical communication terminal suitable for CubeSats
Approach	Direct detection MOPA with 1550 nm downlink. Beacon signal at 976 nm.
Size	$<$ 1.0 kg, 96 mm $\times$ 96 mm $\times$ 119 mm
Power	0.2W (avg transmit power), $<$15 W (consumed power)
Attitude Control	Requires host pointing accuracy of $\pm$ 3 degrees
Beamwidth	1.3 mrad
Downlink Rates	10-40 Mbps
Modulation	PPM

a beacon camera that is sensitive to 976 nm light. The ground station will emit a 976 nm beam that will be used for closed-loop control of the FSM. A secondary feedback laser is also coupled into the collimator and measured with the beacon camera to determine and correct for (with the FSM) any static offsets experienced.

NODE modulates the 1550 nm downlink signal using pulse position modulation (PPM). PPM is used in direct detection systems which do not need to recover the signal phase to demodulate and decode data. Coherent signals measure both the magnitude and phase of the incoming signal but require synchronization between the transmitter and receiver. While coherent systems can allow for better signal-to-noise ratio (SNR) at the receiver, coherent systems require precisely controlled lasers and more complex receivers that are not commercially available [19].

The NODE system is designed to operate for approximately 10 minute periods (the duration of time when the satellite is visible in the sky from a point on Earth). The NODE system will initiate a scanning pattern at the beginning of an operational period to locate the beacon coming from the ground station. After the beacon is found, the fine steering stage will used the measured beacon position to steer the 1550 nm downlink beam to the measure location. The built in feedback laser allows for measurement of system misalignment which will be used to calibrate the pointing system as necessary. Initially, operations will be conducted during the night but eventually operations will be conducted during the day. While night operation allows

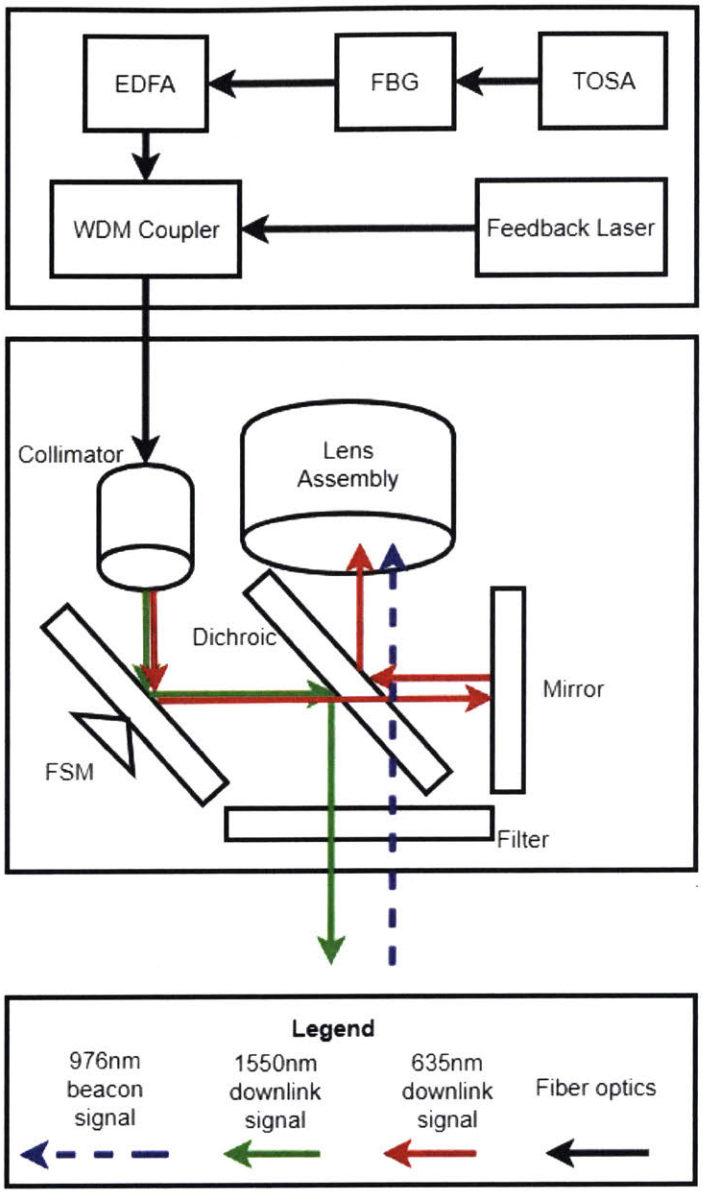

Figure 1-2: Block Diagram of NODE optical system

for better SNR at the receiver, the link budget for the system still closes during daytime operation. The host spacecraft is expected to carry a low-rate RF link that will be used for uplink as well as command and control as necessary. When not in use the system is designed to be remain in a dormant storage mode. More detailed description of the payload operations can be found in [10]. Figure 1-3 depicts a simplified concept of operations.

The NODE system was first formulated in 2013 at MIT Star Laboratory [19]

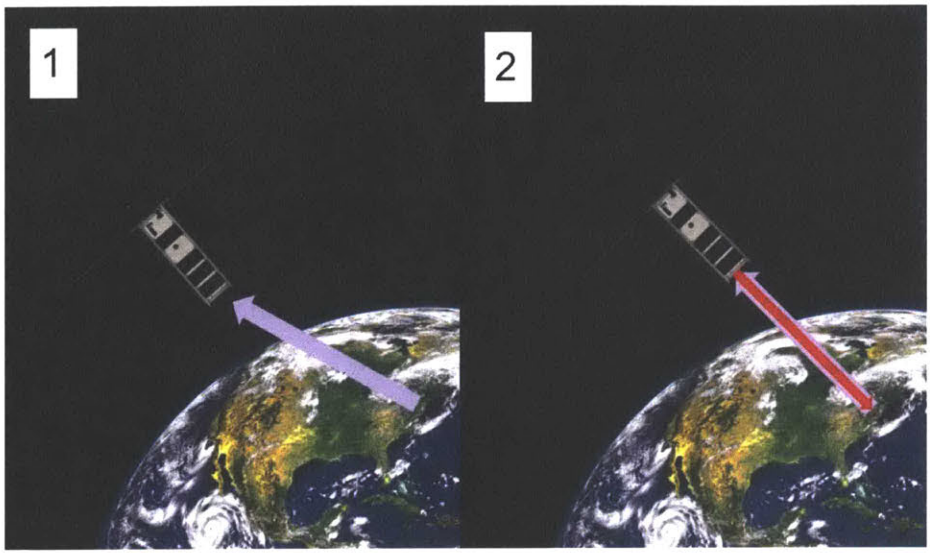

Figure 1-3: Simplified concept of operations. In part 1 host spacecraft points to ± 3 degrees of ground station while the ground station emits 975 nm beacon signal. SC telemetry is transmitted over an RF link. Host initiates a search scan if beacon is not found. In part 2 the beacon signal is measured by NODE payload, and FSM steers emitted 1550 nm beam to ground station. Host slews to follow the ground station over duration of 10 minute downlink. Purple beam indicated 975 nm beacon signal while red signal is 1550 nm downlink beam.

and the payload has progressed in the design life cycle. Pointing capabilities of the NODE fine-steering stage have been verified in a table-top demo [45] and pointing performance of the ground station has also been measured [9] [34] by tracking the International Space Station. Optical analysis has been performed to analyze the effect of misalignments on the opt-mechanical system [26]. The beacon signal has been modeled and simulated with the payload hardware [29].

1.4 Thesis Roadmap

This thesis will discuss the optomechanical design, analysis, and testing of the NODE payload. Specific focus will be payed to structural and thermal subsystems and verification of requirements relating to optical system performance.

Chapter 2 describes the structural and thermal design of the NODE payload. Attention is given to subsystem requirements to maintain optical system alignment and maintain component survival and operational temperatures.

Chapter 3 describes the structural and thermal analysis of the NODE payload performed to verify that the payload meets criteria necessary for mission success. Structural analysis is performed in SolidWorks and thermal analysis is performed in Thermal Desktop.

Chapter 4 describes the experimental testing results of the NODE payload. Payload level vibration testing results are detailed and component level thermal and TVAC testing results are discussed.

Chapter 5 summarizes the work completed, identifies contributions, and discusses required future work on the path to flight of the NODE payload.

Chapter 2

Structural and Thermal Concept Generation and Design

The NODE optomechanical design is driven by mission goals and system requirements [6]. The structure of the NODE payload is designed such that the payload will survive the launch and space environment, maintain alignment of optical elements, support and protect internal components necessary for payload operation, and interface with a host spacecraft. The thermal control system of the NODE payload is designed to keep all payload component temperatures within their operating and survival temperature ranges and ensure that the optical system maintains alignment requirements in the face of thermoelastic shifts caused by the thermal expansion of materials. These two subsystems are highly connected because conduction path, material choices, structural geometry, and optical alignment mechanisms of the payload have effects on structural, thermal, and optical performance.

Margins of safety are a metric that measures how close to failure certain characteristics of a design are. Margins of safety are always desired to be greater than 0 which indicates that the system will not fail. Standard safety factors of 1.25 are used in analysis to add margin. Equation 2.1 is a standard MoS calculation where P_{max} is the maximum load the system can tolerate, $P_{predicted}$ is the predicted load, and SF is the safety factor.

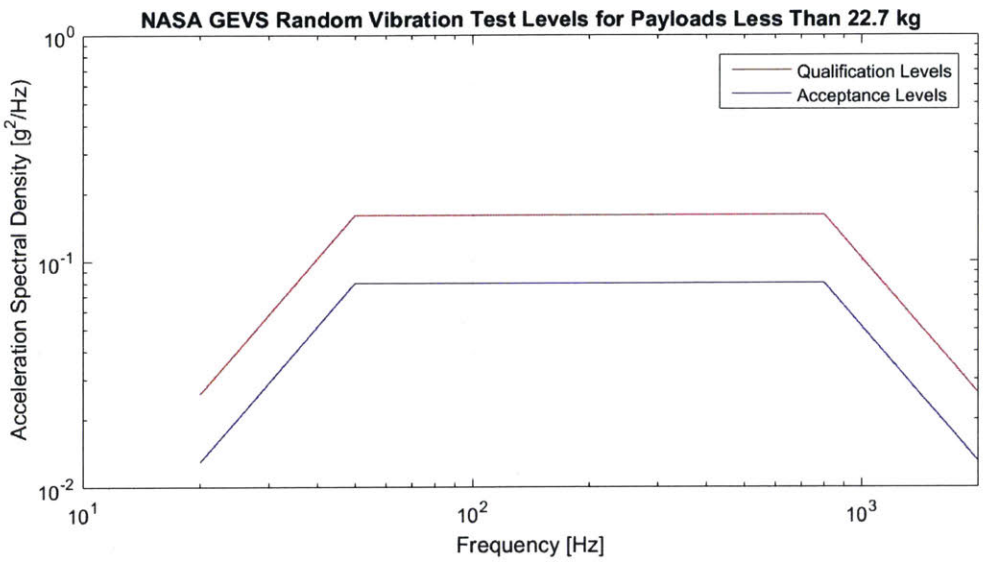

Figure 2-1: Plot of NASA GEVS vibration loads for spacecraft payloads less than 22.7 kg

$$MoS = \frac{P_{max}}{P_{predicted} \times SF} - 1 \tag{2.1}$$

2.0.1 Launch Environment

The launch environment places extreme loads on the satellite and payload caused by vibration, rapid depressurization, and high energy shock impulses (from rocket stage separation and explosive bolts). The payload must survive all of these loads and still be able to meet mission requirements. In order to ensure that the NODE payload is capable of surviving each of these launch loads, the payload is designed to withstand shock and vibrational loads according to the NASA General Environmental Verification Standard (GEVS) [1]. A plot of NASA GEVS qualification and acceptance test loads can be seen in Figure 2-1. The NODE engineering model will be tested to full qualification levels to verify design survivability while the flight unit will be tested to acceptance levels to screen for workmanship errors.

The NODE payload is also be designed to minimize pressure imbalances between the payload and the fairing that occur during launch which place a static load on structural members. The Ariane 5 will be used as a representative vehicle to size

venting holes in the payload as information on the launcher is publicly available from Arianespace [25].

During launch, fasteners that are constraining optics motion can temporarily lose preload and separate, causing shifts in position. Fastener separation analysis should be performed to ensure that the payload optics do not separate and shift during launch. This is only relevant to alignment sensitive free-space optical components, so analyses will only include relevant components.

2.0.2 Space Environment

LEO small satellite missions typically do not exceed 5 years in duration [6]. NODE will be operated in a LEO environment and is expected to be contained within a host spacecraft, radiation damage is not a high concern for the structural or thermal systems, and radiation tolerance is not considered further in this work. COTS component testing indicates that components can survive total integrated doses (TID) of greater than 10 krad(Si) while a CubeSat in a LEO environment can expect a yearly dose of approximately 1.2 krad(Si) [19].

As the specific orbit of the host spacecraft is not yet known, an ISS-like (LEO) orbit is used during the design of the thermal control system. The orbit assumed has an inclination of 51°, eccentricity of 0, orbital altitude of 500 km (higher than the ISS as this is less conservative for thermal analysis), and the right ascension of ascending node is 166° [31]. The thermal control system will manage thermal energy during a cold storage mode in eclipse, as well as operate during a scenario in which the spacecraft and payload system are experiencing maximum thermal energy input. It will be shown that the thermal control system has the ability to support operations between the cold and hot case. Temperatures experienced by the spacecraft in this orbit vary depending on surface coatings, spacecraft power dissipation, surface area, operations, and other factors but are calculated to range from -40°C to 100°° for the NODE payload in section 2.2.1. Figure 2-2 displays the ISS orbit around the Earth.

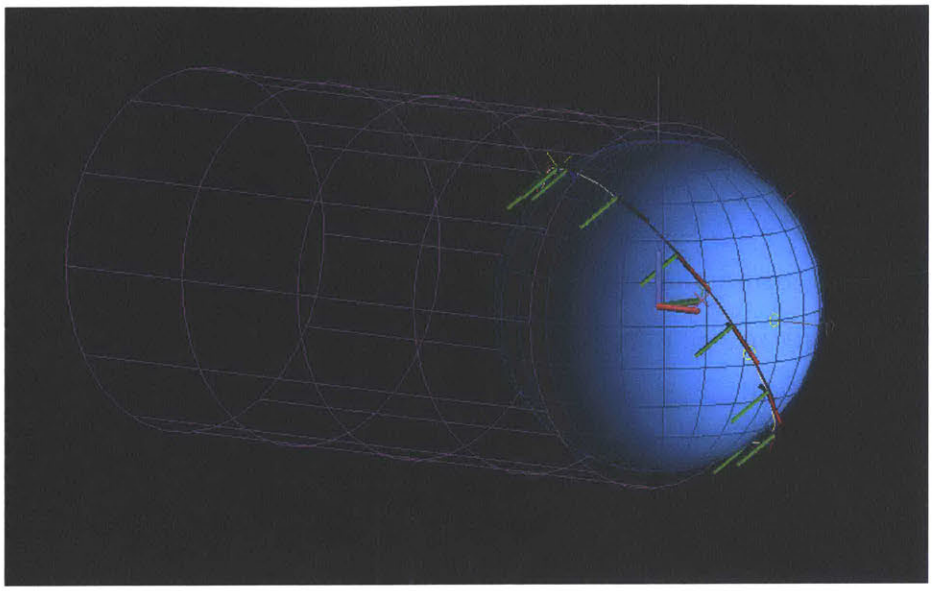

Figure 2-2: ISS orbit used for preliminary thermal design calculations. Orbital height is 400 km.

2.1 Structural Design

In order to be able to meet mission goals, the mechanical design of the payload must be capable of pointing the downlink beam to within 225 arcseconds of the intended orientation [6] before it will miss the receiver. The full-angle beam width of the downlink beam is 2.2 mrad (approximately 450 arcseconds) as defined in the collimator spec sheet [24]. Any experienced thermoelastic deformations caused by coefficients of thermal expansion (CTEs) affect this budget. The structure must also be capable of surviving and retaining alignment after launch and be compatible with host CubeSats.

2.1.1 Structural Design Concept Generation

The NODE payload architecture leverages a wavelength-division multiplexing coupler to add an aligning signal that can be detected on the NODE beacon camera. This allows for the system to be capable of measuring the output beam orientation relative to the beacon orientation and correct for system pointing errors using the FSM. This architecture is tolerant to misalignment in the collimator and FSM, but is sensitive

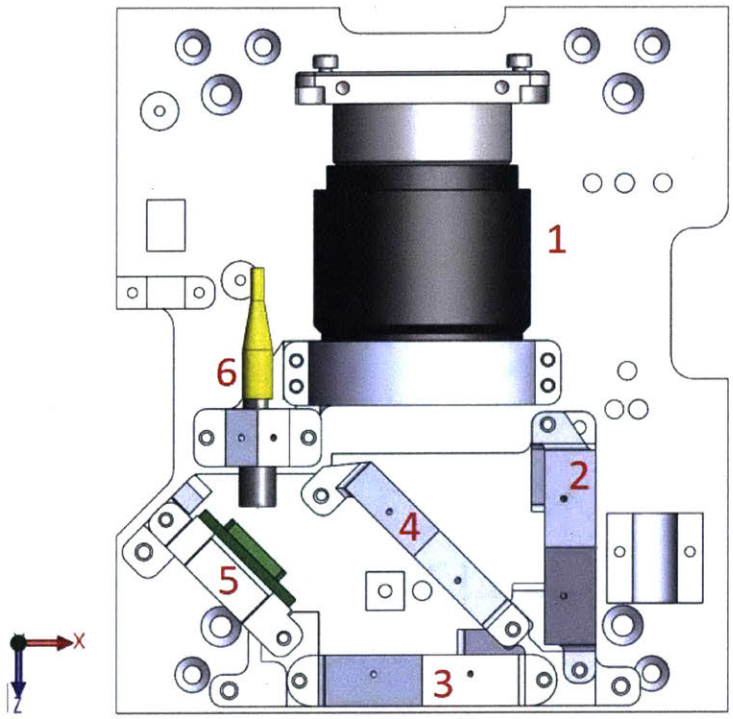

Figure 2-3: Top view of optical elements on NODE payload. Components are 1: Beacon Camera. 2: Mirror. 3: Filter. 4: Dichroic. 5: FSM. 6: Collimator.

to misalignment between the dichroic and the mirror.

Free-space optics are bonded into bezels (discussed in section 2.1.2) with RTV, allowing for the optical elements to be installed beforehand and aligned in their bezels during the last stages of assembly. These optic bezels will be secured into the payload structure and locked with Scotch-Weld 2216 to prevent them from loosening and gapping.

A top view of the optical elements can be seen in Figure 2-3 with significant components indicated. Optical elements are mounted into bezels which are installed onto mounting posts in the structure. The beacon camera is not mounted in a bezel and serves as the reference datum for alignment. The NODE payload will have its single aperture on the +Z face.

The NODE module has a large aluminum optical bench which serves as both the main optical mounting interface and main structural element. While other materials such as carbon fiber, Titanium, and Invar provide better performance (lower

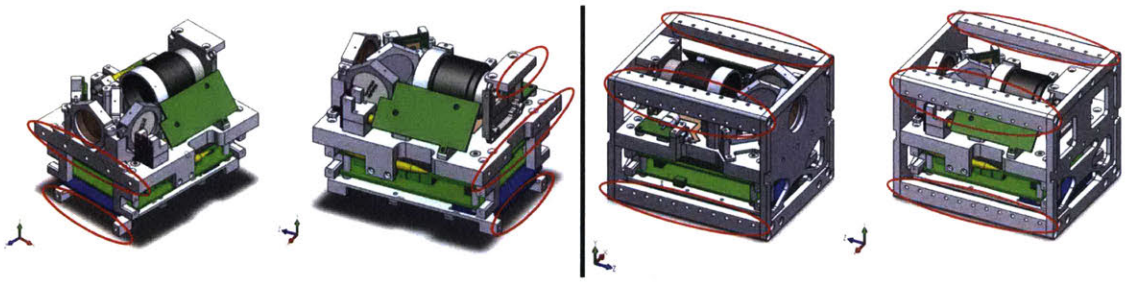

Figure 2-4: Primary and secondary mounting options for NODE.

coefficient of thermal expansion and better stiffness depending on material) than Aluminum, the addition of the alignment signal allows an Aluminum based system to measure and correct for static alignment errors. Materials such as Titanium and Invar are expensive and unnecessary to meet mission goals. The main plate is made of Aluminum T6-6061 alloy as it is commonly available and has a high stiffness yield strength. The main plate serves as the primary mechanical interface to the host spacecraft.

The plate is 96 mm (width) $\times$ 110 mm (length) $\times$ 10 mm (thickness) and is secured to the host spacecraft with M3 fasteners. An alternative mounting structure has been designed that attaches to the main plate and expands the length of the NODE module to 120 mm length, but adds the option of mounting through the module's Y and X faces. Both mounting options can be seen in Figure 2-4 and will be further discussed in Section 2.1.6.

The NODE payload carries seven different PCBs (Table 2.1 list their function) and 10 different wiring harnesses (Table 2.2 lists the components they connect). The largest of the PCBs will be mounted on the -Y face of the payload on standoffs as seen in Figure 2-5. The main optical plate has 3 cutouts where various cables and optical fibers are fed through. All fiber optical components in NODE are spliced together to save space and reduce coupling losses from connectors. These fibers are wrapped around the standoffs and secured in place with fasteners and zip-ties. In-line fiber components are stored on a second fiber optical tray below the PCBs (as shown in Figure 2-5). These in-line fiber components are not sensitive to alignment and therefore have no special mounting requirements other than fiber bend radius

constraints.

Table 2.1: Electronic boards in the NODE payload and their function

Board Name	Function
RPi board	Computational center of NODE, interface with host spacecraft
FPGA board	Implements modulation schemes and coding of laser signal
Daughter board	Interface circuitry and drivers to EDFA, FSM, RTDs, and other components
TOSA board	Houses seed laser and seed laser drivers
Photodiode board	Houses photodiodes
Feedback Laser board	Houses the feedback laser
FSM Board	Houses the FSM

Table 2.2: Cable harnesses in the NODE payload and the components they connect

Cable Name	Component 1	Component 2
E1	TOSA board	FPGA board
E2	TOSA board	Daughter board
E3	Photodiode board	Component 2
E4	Daughter board	FSM Board/Heater 1 & 2
E5	Daughter board	Feedback Laser board
E6	RPi board	Camera
E7	RPi board	Host SC
E8	RPi board	Host SC
E9	RPi board	FPGA board
E10	Host SC	Host SC

The NODE module is designed to not have any large cavities that maintain a pressure differential with the exterior of the payload. Calculations performed in section 2.1.5 predict the pressure differential in the NODE payload.

2.1.2 Optic Mounting

Typical machining tolerances achievable by standard CNC machining range from ± 1 mm to ± 0.002 mm [37]. While it is possible to machine parts up to ± 0.002 mm tolerances, these require special tooling which can be expensive and have long lead

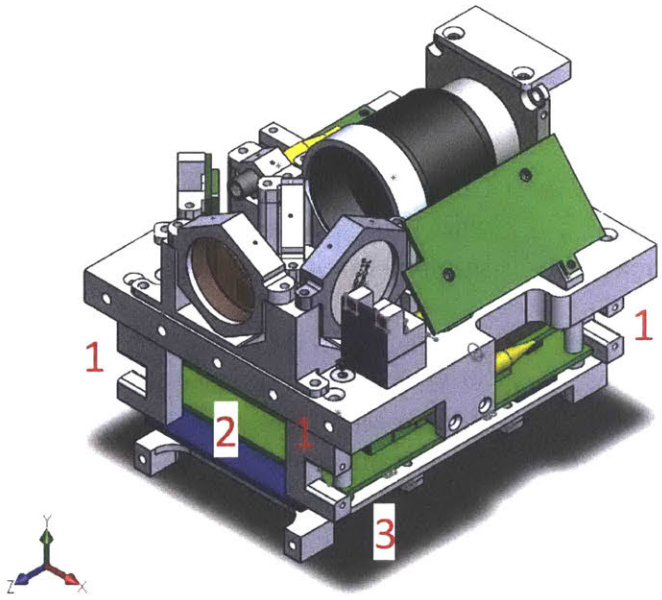

Figure 2-5: NODE PCBs are mounted to -Y face on standoffs. Standoffs are designed to hold excess fiber and ensure minimum bend radius. A second aluminum tray holds in-line fiber components. Standoffs indicated by 1, PCBs indicated by 2. In-line fiber component tray indicated by 3.

times.In this work, it is assumed that machining tolerances of ± 0.13 mm will be achieved on all parts unless otherwise noted [23].

The structural design of the NODE payload is required to allow optical elements to be placed and maintained at a certain orientation and position. Table 2-6 contains a list of required optical alignments for all optical elements. These allowable requirements were determined from modeling performed in Zemax (an optical modeling system) [26]. Previous analysis for worst case alignments given in Table 2.3 is determined to maintain the required optical system performance [26]. In general, there are few alignment requirements in translational position of the optical elements, but there are more strict requirements on the tip and tilt (Rx, and Ry) orientation of the optics as seen in Figure 2.3. Through holes for all bezels are over-sized, allowing for alignment along the X and Z axis for all optics. Machining tolerances of ± 0.13 mm are sufficient to meet all positional requirements listed in Table 2.3 in the Y-axis for all optical elements.

In order to meet tip and tilt alignment requirements in Table 2.3, the optical

Figure 2-6: NODE Components that require alignment for system functionality. Components indicated are 1: Collimator, 2: FSM, 3: Dichroic, 4:Mirror, 5: Beacon Camera, and 6: Filter. Required alignment of each optic is listed in Table 2.3

elements are designed to sit inside bezels which allow for alignment. These bezels are optical mounting tools which allows for optics to be adjusted after bonded by moving the location of the bezel. Figure 2-7 depicts a bezel used to mount the mirror in the NODE payload. Alignment can be achieved by creating oversized through holes which allow for the tilt (Ry) of each optic to be adjusted until it meets alignment requirements. As the tip (Rx) alignment tolerances are not high, standard flatness tolerances achieved by milling bezels allow for tip requirements to be met [42]. After the optic has been aligned to its required position, these bezels are then be fastened into a mounting structure to maintain their alignment. Fastener analysis is performed in a later section 2.1.4.

In order to secure the optical elements to their respective bezels, RTV 566 (an adhesive) is used to bond components. It is possible to mount optical elements with fasteners, however, those fasteners can obscure the optical path, make brittle optics prone to fracture, and apply stresses unevenly throughout the optic [5]. Adhesives

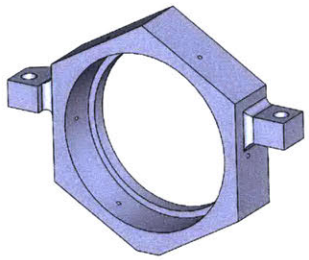

Figure 2-7: NODE optical bezel used to allow for optic alignment adjustment. Optic is bonded into bezel using RTV 566 which is inserted through feed-holes.

Table 2.3: Optical Alignment requirements by component. All alignments are ±

Optical Element Name	Ref Datum	X [mm]	Y [mm]	Z [mm]	Tip [deg]	Tilt [deg]	Roll [deg]
Collimator	FSM	0.18	0.18	-	0.5	0.2	-
FSM	Dichroic	-	-	-	0.25	0.25	-
Dichroic	Beacon Camera	0.18	0.18	0.18	0.25	0.25	-
Mirror	Dichroic	-	-	-	0.25	0.25	-
Beacon Camera	-	-	-	-	-	-	-
Filter	Dichroic	-	-	-	0.25	0.25	-

more broadly distribute stresses and do not obscure the optical path but are subject to drawbacks such as high outgassing and high CTEs that can cause stress to optical elements that experience a wide range of temperatures [5]. RTV has been used in previous missions such as the Transiting Exoplanet Survey Satellite (TESS) which is a MIT-led NASA mission that recently launched [4].

Common optical adhesives include epoxies, urethanes, silicones, UV-cured acrylics, and cyanoacrilates. Epoxies offer high strength bonds but have a high CTE and high Young's modulus which can results in high stress concentrations on optics. Urethanes can be used to create more flexible bonds but should not be used over 100°C [5]. Silicones (such as RTV 566) offer a flexible bond that functions over a wide temperature range and are easy to apply. When bonding with silicones however, the surfaces must be primed and bond curing time can be on the order of days. Finally, silicone bonds have a weak tensile strength and are only recommended for lightweight components

as they can easily fail. Certain silicones have high outgassing values which can disqualify them for space usage. UV-cured acrylics are easy to use, have fast cure times, but require special curing equipment and make weak bonds that could yield during launch. Lastly, cyanoacrylates have a quick cure time and good flexibility, but outgas and have the potential for failure above 71°C [5]. Because the NODE payload only requires small optics to be mounted, will experience a wide range of temperatures, and has outgassing requirements, RTV 566 was selected for its low outgassing qualities, compliant bonds, and ease of application.

In order to verify that RTV 566 optical bonds will not yield during launch, analysis is performed. The optic bezels are all designed such that the only way they can yield will be through shear yielding. For RTV 566, the shear strength G is 3.24e6 Pa. The stress that the individual bond is be exposed to can be found using Equation 2.2 where M is mass of optic, a is acceleration experienced, N is number of bonds, and A is bond area.

$$G_y = \frac{M \times a}{N \times A} \tag{2.2}$$

The most massive optical component in NODE is the mirror which weighs 26 g. The acceleration that the optic will experience will depend on the launch vehicle. It is noted that the Ariane 5 does not experience loads in excess of 4.55g [25], but with added margin the system will be designed to loads of 20 g (a factor of safety of approximately 5). The optic bezels are designed to have 6 bonds of thickness 0.2 mm and area of 7E-6 m^2 (1.5 mm radius).

When solving for the shear stress experienced by each bond, each individual bond will experience 1.2E5 Pa of stress which is approximately 26 times smaller than the shear strength. If we are to assume that 3 of the bonds fail during flight and use a safety factor of 1.25, the optical bonds have a margin of safety of approximately 11.

2.1.3 Resonant Frequency Estimation

One of the main design criteria for the NODE payload is that it must be able to survive the vibrational loading experienced during launch. NASA GEVS state that the minimum resonant frequency of the spacecraft/payload depends on the expected launch vehicle (ELV) [1]. The Ariane V rocket user guide [25] also does not specify a resonant minimum frequency for payloads, but notes that high energy sinusoidal excitations are experienced under 100 Hz and higher frequency vibrations are dominated by acoustic vibration [25]. To avoid resonant coupling between the spacecraft and the rocket, the NODE payload is designed to have a resonant frequency greater than 100 Hz (200 Hz with a factor of safety of 2).

The first frequency of the main plate can be calculated using Equation 2.3 from Roark's Formulas for Stress and Strain [46] which approximates the plate as a beam. This equation assumes that the main plate is fixed at both ends, has a point load W at the center of the plate, has a moment of inertia of I, gravity load of g, length l, and consists of a uniform material with a modulus of elasticity of E.

$$f_1 = \frac{13.86}{2 \times \pi} \times \sqrt{\frac{E \times I \times g}{W \times l^3}} \tag{2.3}$$

When the point load is assumed to be the mass of the payload, $W = Mass \times g$ therefore Equation 2.3 can be simplified to 2.4 where M is the mass of the point load.

$$f_1 = \frac{13.86}{2 \times \pi} \times \sqrt{\frac{E \times I}{M \times l^3}} \tag{2.4}$$

The main plate is made out of Aluminum T6-6061 (as discussed in section 2.1.1) and is assumed to carry all of the mass of the payload ($M = 1$ kg). The modulus of elasticity (E) for Aluminum is 68.9 GPa. In order to accurately calculate the moment of inertia of the main plate, it is modeled as a channel section. A figure of the main plate with dimensions used for modeling can be seen in Figure 2-8. The formula for calculating the moment of inertia in the plate Y axis (drawn with a dotted line in Figure 2-8) is shown in Equation 2.5 [46]. Using 2-8 we can determine d to be 0.007 m, b to be 0.096 m, t_w to be 0.012 m, t to be 0.003 m, and y_c to be 0.005 m (the

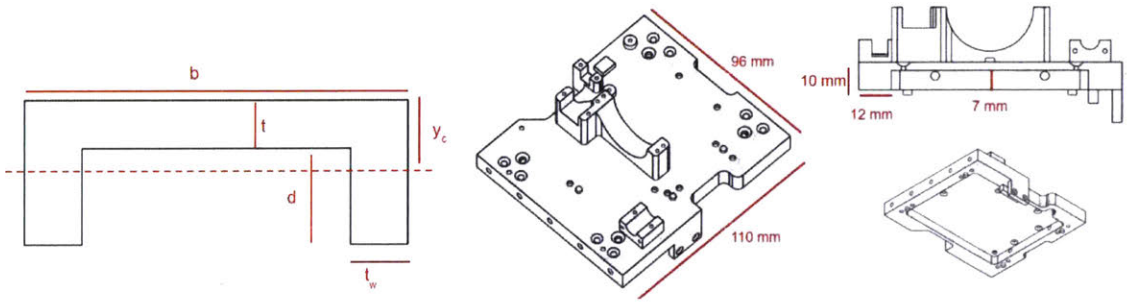

Figure 2-8: Dimensions of NODE main plate structure for resonant frequency calculations. Channel section dimensions drawn on left chart indicate critical dimensions for calculations.

distance to the fastener holes).

$$I = \frac{b}{3} \times (d+t)^3 - \frac{d^3}{3} \times (b - 2 \times t_w) - A \times (d + t - y_c)^2 \tag{2.5}$$

Solving for the moment of inertia I, it is found to be 1.23E-8 kg m^2. Solving for the first resonant frequency of the main plate using Equation 2.4 it is found that the first frequency of the plate is approximately 2000 Hz. This exceeds the minimum target frequency of 200 Hz by a factor of 8, however, it is worth noting that while the main plate may have a high first frequency, mounted PCBs will likely have a lower first frequency due to their large area, lower modulus of stiffness, and standoff mounting scheme. The resonant frequency of mounted components is determined computationally in section 3.1.2.

2.1.4 Fastener Analysis

In order to verify that optical elements remain aligned after launch and fastener connections do not yield to shear or tensile loads, analysis is performed on the heaviest optical element to ensure that margins of safety are positive.

In order to verify that secured optical components remain in place, analysis is performed to show that bolted joints of optical components never separate. The analysis methodology is derived from the NASA Preloaded Joint Analysis Methodology for Space Flight Systems Memorandum [3].

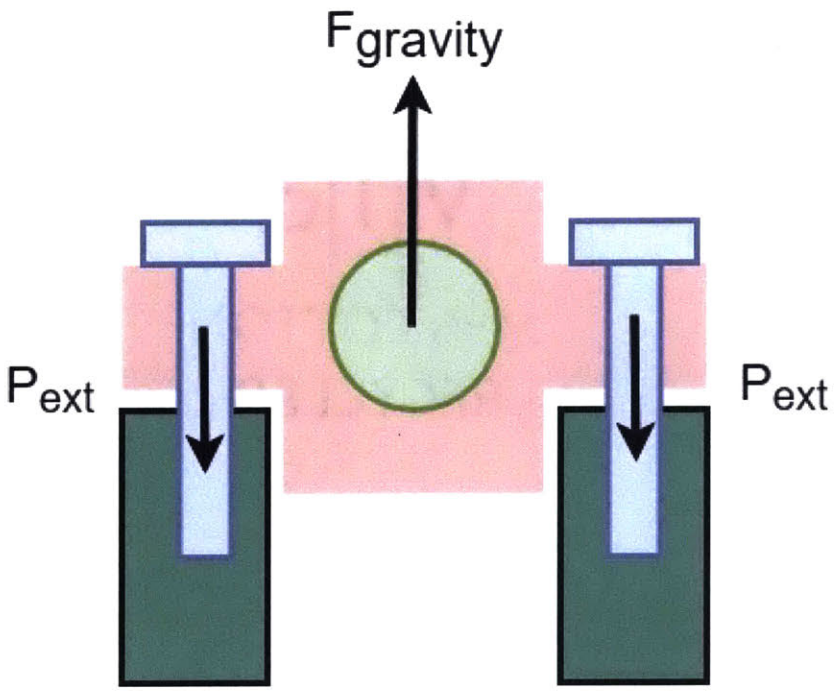

Figure 2-9: Free body diagram used to calculate P_{ext}. In the scenario in which the body experiences no acceleration, the screws support the full gravity loading of the optical element.

In order for a bolted joint to never separate, it must never exceed its separation load (compressive preload of fastener must never be overcome by external tensile load). The separation load of a bolted joint can be calculated as seen in Equation 2.6 where P_{ext} is the external load applied, ϕ is the joint stiffness factor, and n is the loading plane factor.P_{ext} can be found by creating a free-body diagram. Figure 2-9 shows the free body diagram used to calculate P_{ext}. If the optical element is not accelerating, the loading the fastener experiences can be found using Equation 2.7 where m is the mass of the optical element, g_n is the gravity loading, and $N_{fasteners}$ is the number of fasteners constraining the optical element .

$$P_s = (1 - n * \phi) * P_{ext} \tag{2.6}$$

$$P_{ext} = m \times g_n / N_{fasteners} \tag{2.7}$$

The calculated shear margin for a fastener can be found using Equation 2.8, where

P_o is the minimum expected preload and SF_s is the safety factor for separation.

$$MS_{separation} = P_o/(SF_s \times P_s) - 1 \tag{2.8}$$

The shear margin for a fastener connection is calculated by determining the shear stress exerted on the fasteners and comparing to the stress at which the fastener would begin to yield. Equation 2.9 [3] is used to calculate the shear margin for the individual fasteners where $V_{allowable}$ is the maximum allowable shear stress, SF_{shear} is a safety factor for predicted shear loading (1.25 is used), and V is the predicted experienced shear loading. The predicted shear stress experienced V can be calculated with a free body diagram where internal screw forces oppose gravity forces expected during launch.

$$MS_{shear} = V_{allowable}/(SF_{shear} \times V) - 1 \tag{2.9}$$

The tension margin for a fastener connection is calculated by determining the shear stress exerted on the fasteners and comparing the stress at which the fastener would begin to yield. Equation 2.9 [3] can be used to calculate the shear margin for the individual fasteners where $V_{allowable}$ is the maximum allowable shear stress, SF_{shear} is a safety factor for predicted shear loading (1.25 is used), and V is the experienced shear loading.

$$MS_{tension} = T_{allowable}/(SF_{tension} * T) - 1 \tag{2.10}$$

Analysis is performed on the heaviest optical element which is the mirror. The mirror is secured with two fasteners (M2 18-8 Stainless Steel) which are staked with 2216 in the threads. The loading plane factor for the optical mounting configuration is calculated to be 0.75, the joint stiffness can be found to be 3.64E8 newton-meter, and external load applied is found to be 3.2 newtons. Detailed calculations for these numbers are available in Appendix A and are omitted here. The separation load P_s is calculated to be 2.8 Newtons, and the margin of safety for separation is found to be approximately 200. When the shear and tensile margins of safety are found for

the same optic, they are found to be approximately 350 and 500 respectively. Table 2.4 displays all calculated margins of safety for the mirror. As this is the heaviest optical element, it is assumed all other optical elements have higher margins and will not separate or yield due to tensile or shear loads.

Table 2.4: Calculated Fastener margins for heaviest optical element (Mirror)

Analysis Type	Predicted Margin of Safety
Tension	400
Shear	350
Separation	200

2.1.5 Depressurization Design

NASA GEVs requires analysis to show that the spacecraft/payload does not experience any significant pressure gradients during launch that could cause structural failure. Analysis is performed to model the internal pressure of the NODE payload with a representative fairing pressure profile and examine the worst case predicted force on optical components. It is assumed that additional internal volumes that exist in the assembly (such as trapped pockets of air in fastener joints) are small and will not produce a significant pressure differential.

The pressure differential between an enclosed volume V with a venting orifice area A with a ambient fairing pressure P_o is calculated using Equation 2.11 [38]. Detailed calculations can be found in Appendix A.

$$\triangle P = \frac{1}{2 \times g \times R \times T} \times (\frac{V}{A \times C})^2 \times (\frac{dP}{dt})^2 / P_o \tag{2.11}$$

A representative pressure profile is generated from data in *Spacecraft Compartment Venting* [38] and can be seen in Figure 2-10 along with the predicted NODE payload pressure. Because the NODE payload has four open faces, it is assumed that the venting area will be provided by the host spacecraft. Analysis assumes that the host spacecraft provides a 1 mm $\times$ 1 mm rectangular cutout for venting. While this is a small venting hole, it is used as a worst case scenario.

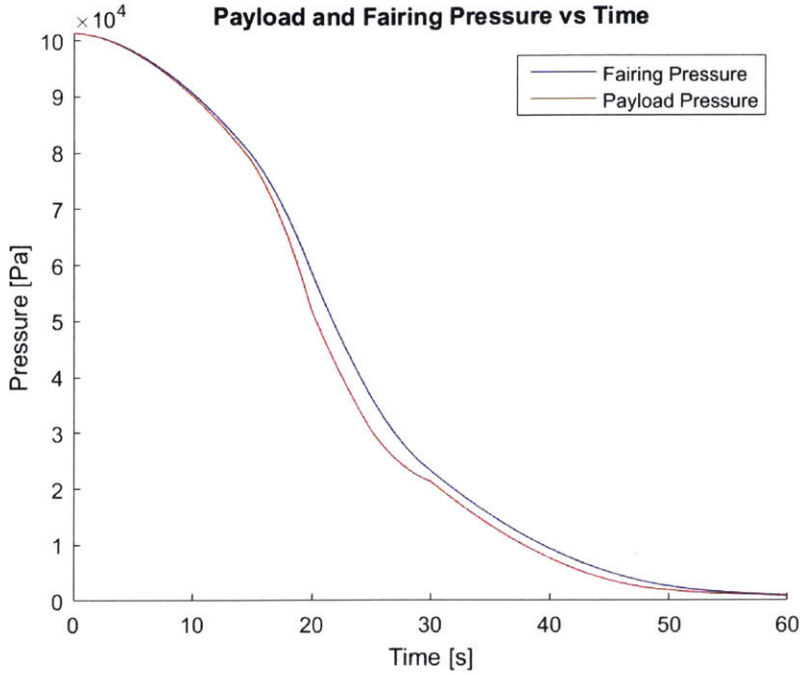

Figure 2-10: Predicted pressure profile of fairing and NODE payload during launch.

The predicted pressure difference between the rocket fairing and NODE payload can be seen in Figure 2-11. If it is assumed all 7000 Pa of pressure are acting upon the area of the mirror, we can calculate the induced stress on a single RTV bond to be 8.1E4 Pa using Equation 2.12 where A_{optic} is the area of the optical element, $Pressure_{max}$ is the maximum pressure differential experienced by the element,A_{bond} is the area of an individual RTV bond, and N_{bonds} is the number of RTV bonds for the optic. If we assume this pressure load acts in the same direction as the gravitational load calculated in the Section 2.1.4, a margin of safety of 13 is calculated for all 6 adhesive bonds, and a margin of safety of 5 (assuming a safety factor of 1.25 in each case) in the scenario that 3 adhesive bonds fail by adding the $P_{pressure}$ stress to the gravity load stress calculated in Section 2.1.4. These margins of safety are positive and are deemed sufficient.

$$P_{pressure} = \frac{A_{optic} \times Pressure_{max}}{A_{bond} \times N_{bonds}} \tag{2.12}$$

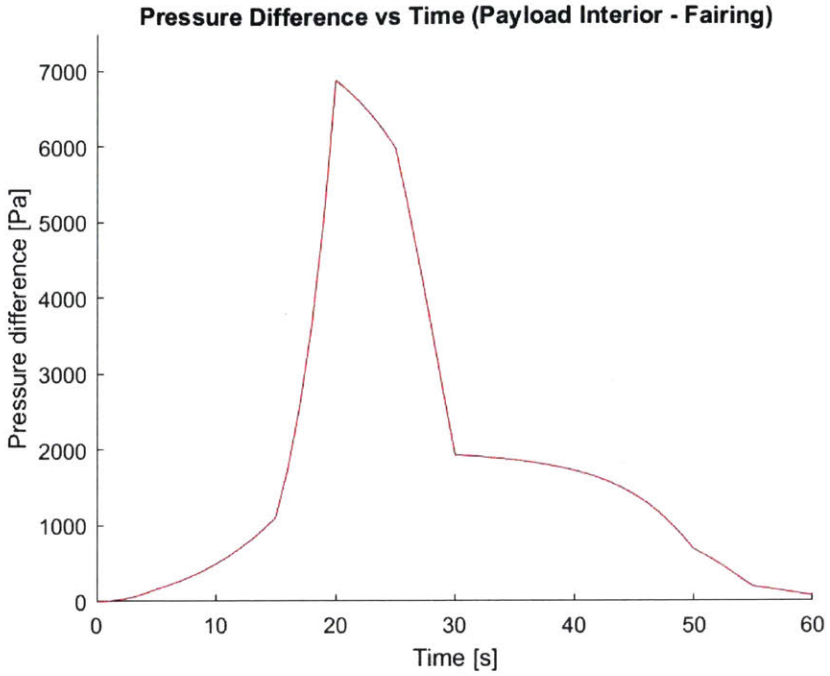

Figure 2-11: Predicted pressure difference between fairing and NODE payload during launch.

2.1.6 Interface With Host Satellite

The NODE payload is designed to interface with a large variety of CubeSat hosts. In order to be accommodate different mounting needs, the NODE payload is designed to have multiple mounting configurations. As discussed previously, the NODE payload can be mounted to the host directly through the main optical plate on both the +Z and -Z faces of the payload in what will be referred to as the "direct mounting" configuration, as seen in Figure 2-12. This mounting configuration removes the need for extra mounting structure and is preferred due to the size and mass savings (compared to other mounting schemes). Vibrational modes of the main plate calculated in section 2.1.3, computational analysis performed in section 3.1, and thermal analysis performed in section 3.2 are calculated using the "direct mounting" configuration.

Other alternative mounting configurations require addition of mounting interface hardware to the +Z and -Z faces and corner rails of the module in what will be called the "mounting cube" configuration. Additional end plates are added to the system that are used to mount rails with regularly spaced threaded holes. These threaded

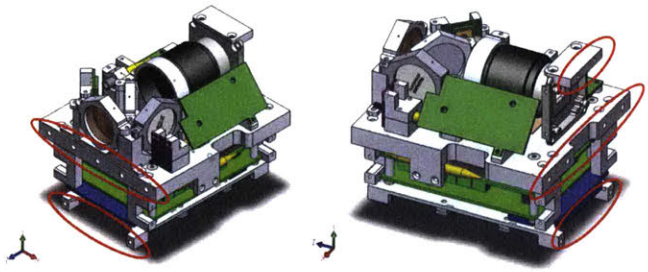

Figure 2-12: NODE mounting configuration through +Z and -Z faces. Required fastener location is circled. Analysis in Sections 2.1.3, 3.1, and 3.2 assumes this mounting configuration.

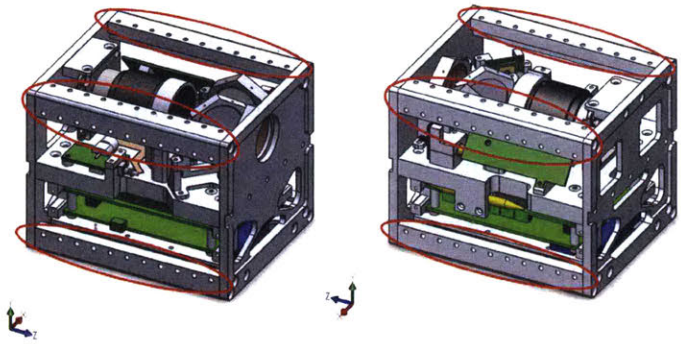

Figure 2-13: NODE mounting configuration through +X,-X,+Y,and-Y faces. Potential locations for fasteners are circled. Only a subset of threaded fastener connections necessary for mounting.

holes allow for a variety of mounting options as not all threaded holes are required. This allows for host satellites to determine the location in which fasteners are inserted. All analysis performed in this thesis assumes the NODE payload interfaces with the satellite through the "direct mounting" configuration and not through the "mounting cube" configuration. If NODE is integrated in the "mounting cube" configuration, analysis should be updated to reflect changes in boundary conditions, and is listed as future work for this thesis.

Cables and harnesses are routed through the -Z face of the payload and both configurations allow for access to the host electronics and power sources.

2.2 Thermal Design

A complete list of all components with their survival and operating temperature ranges is shown in Table 2.5. Components that have the lowest maximum temperature (for both operational and survival) and highest minimum temperature (for both survival and operational) will drive the thermal control system (TCS) design. For NODE, the beacon camera satisfies both of these conditions and will be the driving component. The payload optical system must maintain the optical output beam alignment to within 225 arcseconds (accounting for thermoelastic effects) [6] [24] before the beam will miss the ground station as discussed in section 2.1. The thermal design is conducted by identifying the hot and cold scenarios that the payload will experience and designing the payload to operate in both scenarios. As the host of the payload is currently unknown, conservative estimates are made when identifying both scenarios. The thermal control system must maintain operational and survival temperature ranges for all mission cases. Thermoelastic effects on system pointing are analyzed during a nominal operations case intended to be representative of typical payload operations.

Table 2.5: Component survival and operational temperature ranges

Component Name	Survival Min Temp	Survival Max Temp	Operational Min Temp	Operational Max Temp
EDFA	-40°C	85°C	0°C	70°C
APD	-40°C	85°C	-40°C	85°C
Fiber Components	-40°C	85°C	0°C	70°C
Collimator	-35°C	80°C	0°C	70°C
Beacon Camera	-20°C	60°C	0°C	45°C
TOSA	-40°C	85°C	-5°C	75°C
Electronics	-25°C	65°C	0°C	60°C
Pi Board	-25°C	80°C	-25°C	80°C
Feedback Laser	-35°C	80°C	0°C	75°C

2.2.1 Single Node Model and Identification of Hot and Cold Cases

In order determine a first order calculation of expected temperatures onboard the NODE payload, a single node model of the spacecraft is developed. The model is used to determine steady state temperatures for bounding cases, verify later modeling results, and identify hot and cold cases for the spacecraft.

In order to identify the steady state temperature of the spacecraft, all heat flows in and out of the spacecraft system are identified. In a steady state case, the heat flow into the spacecraft is equal to the heat flow out of the spacecraft. This is represented mathematically in Equation 2.13.

$$\frac{Q_{in}}{dt} = \frac{dQ_{out}}{dt} \tag{2.13}$$

Heat flows into the system include spacecraft internal heat generation, payload internal heat generation, and radiative sources of heat (planet shine, albedo, and solar radiation) which are evaluated on a face-by-face basis. Radiative heat flows out of the system are evaluated on a face-by-face basis by approximating the spacecraft as a grey body using the Stefan-Boltzmann law. It is assumed that other sources of energy flow out of the system (such as with lasers or RF communications systems) are small and will not be included in analysis.

Assuming that the host spacecraft is a 3U CubeSat in a 500 km orbit with a 51 degree inclination, has double deployable solar panels, and has Alodined aluminum body surfaces, we can adjust Equation 2.13 to make it into the more explicit form in Equation 2.15. Solving explicitly for T, temperature of the spacecraft we can find the steady state temperature of the spacecraft. Note that Equation 2.15 assumes that all faces are orthogonal to the normal vector of that surface and the celestial body that they are radiating to/from.

$$Q_{SC}+Q_p+J_s\times\alpha\times A_{sun}+J_s\times VF_aC_a\times\alpha\times A_p+J_{ps}\times VF_{ps}\times\epsilon\times A_p=\epsilon\times\sigma\times A_{SC}\times T_{sun}^4 \tag{2.14}$$

$$T_{sun}=(\frac{Q_{SC}+Q_p+J_s\times\alpha\times A_{sun}+J_s\times VF_a*C_a\times\alpha\times A_p+J_{ps}\times VF_{ps}\times\epsilon\times A_p}{\epsilon\times\sigma\times A_{SC}})^{1/4} \tag{2.15}$$

When the spacecraft is in eclipse, it experiences no thermal input in the form of solar radiation or albedo. The steady state temperature of the spacecraft in eclipse is calculated using Equation 2.16. Again, note that all faces are orthogonal to the normal vector of that surface and the celestial body that they are radiating to/from.

$$T_{ecl}=(\frac{Q_{SC}+Q_p+J_{ps}\times VF_{ps}\times\epsilon\times A_p}{\epsilon\times\sigma\times A_{SC}})^{1/4} \tag{2.16}$$

Based on the spacecraft CONOPS, four cases are analyzed to identify the hot and cold cases for the NODE payload. For the hot case, analysis is performed to identify the temperature of the spacecraft in a hot storage mode and hot operational mode. The hot storage mode models expose maximum spacecraft area to both the sun and the planet which maximizes the incoming radiative thermal energy, but assumes that the payload is not operating (the NODE payload will never down-link when not nadir pointing). The hot operational mode assumes the spacecraft is nadir pointing (minimizing the radiative heat flows into the system), but maximize the internal payload heat generation. For cold cases, an eclipse storage mode and eclipse operational mode is considered. For the storage mode, it will be assumed the spacecraft is exposing the maximum area to earth to maintain temperature, but it is not operating the payload. Finally, the eclipse operational mode is nadir pointing, but is operating at full payload power. Table 2.6 compares different cases under examination and their predicted temperatures. Detailed calculations and assumptions with values used are available in the appendix.

Based on the predicted temperatures seen in Table 2.6 it appears that a thermal

Table 2.6: Thermal Cases under Examination

Case Name	Nadir Pointing	Payload Operational	Predicted Temp [°C]
Hot Storage	No	No	100
Hot Operational	Yes	Yes	-30
Eclipse Storage	No	No	-30
Eclipse Operational	Yes	Yes	-40

control system is necessary to keep components within their operational and survival temperature limits. While this 1-node model is an approximation and does not incorporate internal conductive or radiative heat transfer, transient behavior, or spacecraft thermal management through a thermal control system or spacecraft CONOPS, it is used to inform the design of the thermal control system and bound later computational models.

2.2.2 Thermoelastic Deformations

The payload optical system can tolerate up to 125 mrad misalignment including thermoelastic expansion before the downlink beam misses the ground station [6]. Hand calculations are performed in order to estimate experienced thermoelastic misalignments.

As the beam is collimated and remains collimated after the exit of the collimator, shifts in optical length between optics have no effect on system performance and thermoelastic effects are not considered. Due to the addition of the aligning beam, thermoelastic effects experienced on the collimator, FSM, dichroic, and beacon camera can be measured and corrected for as long as the beam does not miss an optic (the tightest requirement will be on the FSM). Alignment that can not be calibrated out of the system is alignment between the field mirror and the dichroic. These two cases are analyzed with the mechanical structure.

When determining the thermoelastic effects between the mirror and dichroic, the geometry between the two optics is analyzed. Figure 2-6 shows both the aluminum mounting structure and simplified geometry used to calculate induced thermoelastic misalignment. In order to estimate the tilt error between the two optics, the worst

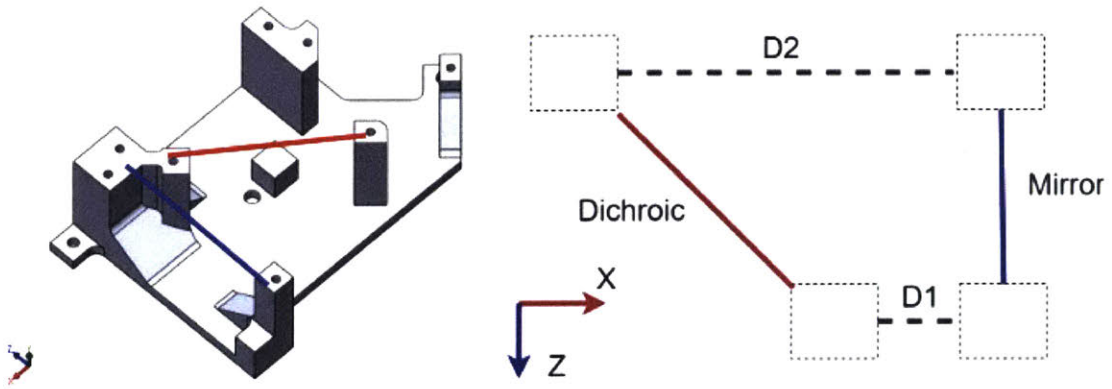

Figure 2-14: Left: CAD image of optical mounting plate. Right: Simplified geometry used to calculate angular shifts caused by thermoelastic deformation.

case change in D1 and D2 is found based on material CTE and temperature gradient. Equation 2.17 is used to calculate the change in length between two structures with a uniform material and given Δ T.

$$\Delta D = D_n \times \Delta T \times CTE \tag{2.17}$$

Looking at the simplified geometry, the tilt misalignment is found using equation 2.18. Solving for the experienced thermoelastic tilt misalignment, it is found to be 0.09 mrad if we assume a 5 degree Δ T across D2 (causing expansion) and a -5 Δ T across D1 (causing compression). This is well within the 103 mrad required.

$$\theta_{misalignment} = |\tan^{-1}\frac{D2 + \Delta D2 - D1 - \Delta D1}{D_{mirror}} - \tan^{-1}\frac{D2 - D1}{D_{mirror}}| \tag{2.18}$$

When examining the tip requirement, thermoelastic effects that drive misalignment are caused by thermal gradients across individual mounting mounting posts (one side of the post expands while the other compresses). Equation 2.19 is used to calculate a tip misalignment of 0.1 mrad which is significantly less than 103 mrad. Detailed calculations for both can be found in Appendix A.

$$\theta_{misalignment} = |\tan^{-1}((\Delta D1 + \Delta D2)/D_{postwidth})| \tag{2.19}$$

2.2.3 Thermal Control System Concept Generation

In order to meet mission requirements, the NODE payload must keep its internal components within their required operational and survival temperature ranges. Because the specific orbit and host spacecraft are unknown, reasonable estimates are made assuming the payload environment and the NODE thermal control system will be designed to support expected mechanical interfaces and thermal boundary conditions.

From the 1-node model developed in the previous section, we can identify scenarios that will be the most taxing upon the designed thermal control system. During operational modes, the beacon camera has the highest minimum operating temperature of 0°C which is above the predicted temperature for both operational modes. During eclipse storage it appears that the predicted temperature (seen in Table 2.6 will fall below minimum survival temperatures for the beacon camera. While in direct sunlight storage mode, the payload will be too hot for every component based on Table 2.6.

Design of the thermal control system for NODE first requires identification of all potential strategies for thermal management. It is unlikely that the host spacecraft will be able to change its surface coatings or passive thermal management system (by adding additional radiative thermal control devices or heaters), but it is assumed that internal mechanical and thermal interfaces can be changed as necessary to meet NODE mission requirements. It is also assumed that small changes in spacecraft operations are acceptable in order to meet NODE mission requirements.

The NODE payload also has a payload-level thermal management system. When identifying potential options to manage heat transfer, passive options such as conductive heat straps and surface coatings, as well as active thermal management hardware such as heaters, are considered.

Looking at the predicted steady state temperatures in Table 2.6, it is possible to lower the maximum expected temperature of components by limiting spacecraft power dissipation and thermally isolating the payload from the hottest parts of the

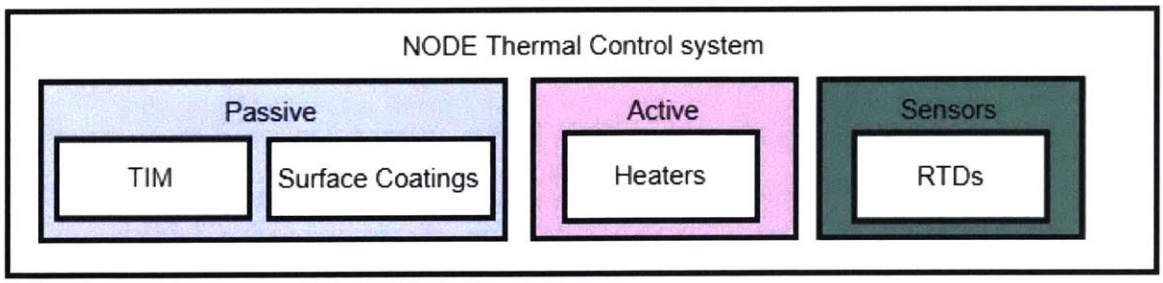

Figure 2-15: Thermal Control System for NODE payload

spacecraft (likely the solar panels).In the cold cases, additional payload heaters, thermal isolation, and surface coatings (when chosen correctly) cause the temperature of the payload to be higher than that of the spacecraft when moving to a multi-node model (analysis performed computationally in section 3.2). If correctly sized, the combination of heaters and thermal isolation material (TIM) should allow for the NODE payload to operate locally at a higher temperature than the spacecraft bus.

Exact sizing and implementation of heaters and TIM are determined using a Thermal Desktop Model with the goal of identifying heater and TIM size and location as well as the appropriate surface coatings in section 3.2. Resistance Temperature Detectors (RTDs) are used to sense component temperatures for heater control. Figure 2-15 displays the passive and active components of the proposed thermal control system as well as the selected sensors of the proposed NODE TCS.

Chapter 3

Structural and Thermal Analysis

After developing a preliminary design concept for the NODE structural and thermal systems, analysis is performed to prove that requirements are met in all expected operational modes. Margins of safety are also analytically determined in order to show that the system meets requirements even in cases where modeling uncertainty exists.

3.1 Structural Analysis

In order to verify that the proposed NODE design meets structural requirements, Finite Element Analysis (FEA) is performed in SolidWorks to computationally determine the natural frequency and safety factor for static loads experienced during launch. After analysis is performed, the results are validated by comparing to hand calculations from Chapter 2.

3.1.1 FEA Model

A Finite Element Mesh (FEM) is developed in Solidworks as a representative model of the mechanical structure of the payload. The model is developed incrementally and hand calculations aree performed at intermediate modeling steps to validate modeling accuracy. Figure 3-1 shows the NODE FEM and boundary conditions used

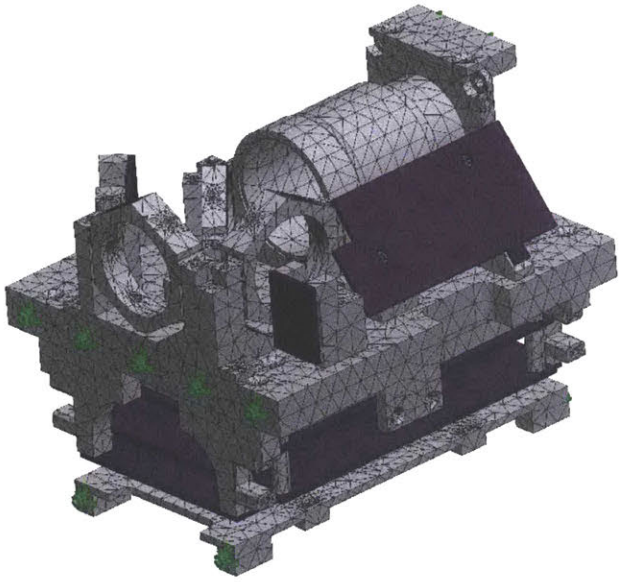

Figure 3-1: NODE Structural Finite Element Mesh used for analysis. Aluminum components indicated in gray while PCBs are displayed in purple. Green arrows indicate boundary conditions. Solidworks simulation files available in STAR Lab NODE repository.

for analysis.

Boundary conditions are assumed to be the mounting interfaces with the host spacecraft. All analyses are performed assuming the "direct mounting" configuration from section 2.1.6 and FEA is not performed for the "mounting cube" configuration. Optics and other components (such as PCB-mounted components) are not included in the model as their mass is small and not expected to contribute significantly to results.

3.1.2 Resonant Frequency Analysis

Finite element analysis (FEA) is performed using the finite element model to determine the first resonant frequency of the NODE payload (and identify the location). It is not expected that the main plate will contain the component that has the lowest first frequency, but rather it is expected that the first resonant frequency will be experienced at thin PCBs or optic mounts that are mounted in a cantilever fashion.

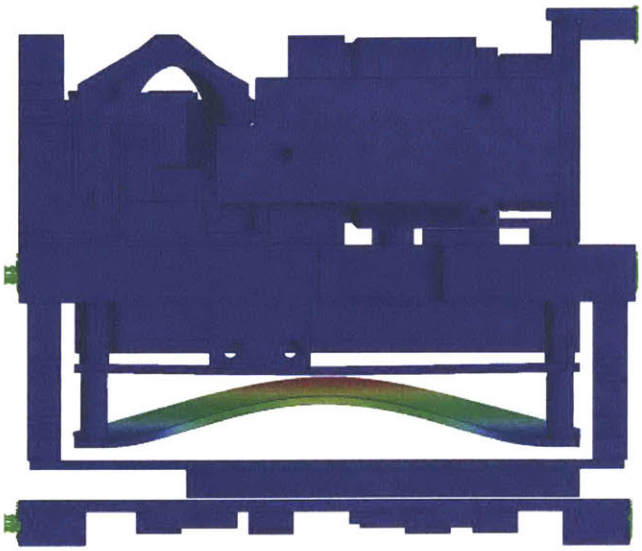

Figure 3-2: First frequency of NODE payload is predicted to be at 500 Hz at FPGA board. Drum motion is expected.

After components that have a first low frequency are identified, the analysis is be used to inform location of accelerometers used in vibration testing for later validation of results.

As expected, analysis predicts that the first resonant frequency of the NODE structure is not located at the main structural plate, but rather is located at a smaller component. Analysis predicts that the first resonant frequency of the payload is approximately 500 Hz at the FPGA board. Figure 3-2 depicts the drum resonance expected at the FPGA board. The second resonant frequency is expected to be located at the daughter board and is expected to occur at approximately 500 Hz. The second resonant frequency is shown in 3-3.

The third resonant frequency is expected to occur at 700 Hz at the Raspberry Pi board while the fourth and fifth frequencies are second order resonances on the FPGA and daughter board respectively. Predicted frequencies of other components such as the main plate, coupler tray, and optic mounts are listed in Table 3.1. All predicted resonant frequencies are above 200 Hz which is the desired minimum frequency as discussed in section 2.1.3. The expected first frequency of the payload of 500 Hz exceeds the minimum design goal of 200 Hz by a factor of 2.5. The computationally predicted

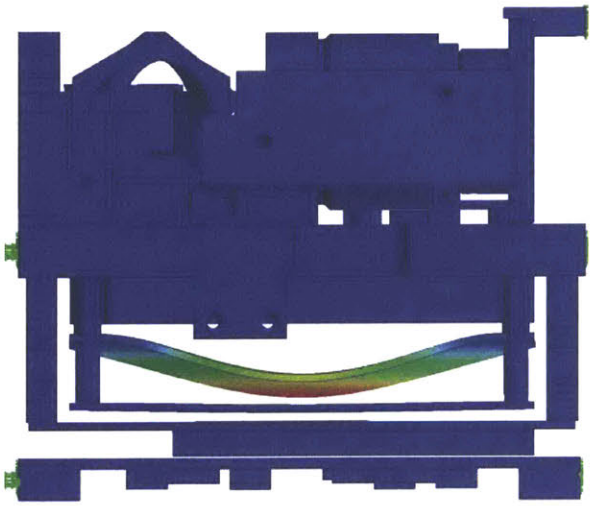

Figure 3-3: Second frequency of NODE payload is predicted to be at 500 Hz at daughter board. Drum motion is expected.

first frequency of the main structure is 2100 Hz while hand calculations predicted a first frequency of approximately 2000 Hz. The hand calculations and computational model results differ by about 5%, adding confidence to modeling results.

Table 3.1: Predicted resonant frequencies of NODE structure, locations, and harmonic.

Order of Resonance	Location	Frequency [Hz]	Harmonic (direction)
1	FPGA Board	500	1
2	Daughter Board	500	1
3	Raspberry Pi Board	700	1
4	FPGA Board	900	2
5	Daughter Board	900	2
-	Coupler Tray	1000	1
-	Coupler Tray	1700	2 (x)
-	Main Plate	2100	1
-	Coupler Tray	2100	2 (z)
-	EDFA	2900	1

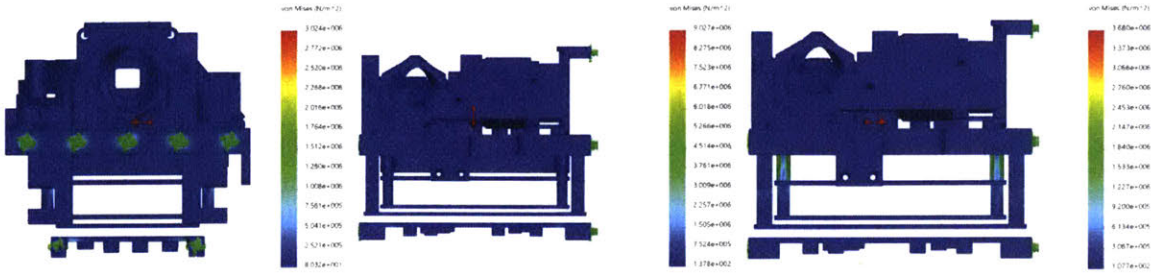

Figure 3-4: Static loading analysis results in X, Y, and Z axis respectively.

3.1.3 Static Loading Analysis

Static load analysis is performed on all three axes of the payload to a load of 20 g's. This analysis is performed to examine the stress on structural components to determine if they will yield. Optical components and fasteners are not included in this analysis as previous hand calculations in Chapter 2 indicate a sufficient margin of safety.

The structure of the spacecraft is nearly all aluminum 6061 T6 which has a tensile yield strength of 2.76E8 Pa and a shear yield strength of 2.07E8 Pa [16]. In order to calculate the margin of safety for static loading, Equation 3.1 is used (margin of safety equation is explained at the start of Chapter 2), where $P_{staticyield}$ is the tensile or shear yield strength of the structural material, SF_{static} is the safety factor for static loading (1.25), and $P_{staticpredicted}$ is the predicted static loading determined from SolidWorks static loading analysis.

$$MS_{static} = \frac{P_{staticyield}}{SF_{static} * P_{staticpredicted}} - 1 \tag{3.1}$$

Analysis predicts maximum stresses of 3E6 Pa, 9E6 Pa, and 4E6 Pa in the X, Y, and Z axis respectively. Table 3.2 displays the predicted loads and safety factors for each axis while Figure 3-4 graphically depicts the location of the maximum loading. Where the maximum load was predicted to be on a PCB, the margin of safety is calculated for FR-4 which has a lower yield strength. Margins of safety are predicted to be greater than 5 for all axis.

Table 3.2: Predicted static loads and margin of safety for NODE payload in each axis.

Axis	Maximum Stress [Pa]	Load Type	Margin of Safety
X	3e6	Shear	50
Y	9e6	Tensile	20 (aluminum) / 5 (PCB)
Z	4e6	Shear	40

3.2 Thermal Analysis

In order to size thermal control system characteristics and verify that the NODE payload meets thermal system requirements, a Thermal Desktop model is developed. The Thermal Desktop model is a mathematical model that calculates internal and external radiation, simulates the space environment to predict environmental thermal loads on the spacecraft, models internal conduction paths between the host spacecraft and the payload, and simulates performance of thermal control system components and control laws (ex: heaters and their set points and gains).

The payload can be mounted in multiple configurations which all have different thermal paths. The thermal analysis models the payload in the "direct mounting" configuration discussed in section 2.1.6. This mechanical interface is common to all mounting configurations and TIM can be applied to this connection regardless of mounting configurations. If the NODE payload is mounted to the bus through the exterior mounting rails, it should be verified that the payload stays within operational temperature ranges for the specific mounting configuration.

The hot and cold cases for both operational and storage modes are identified by analysis in section 2.2.1 and are the scenarios in which the thermal control system will be proven to meet mission requirements. These cases are expected to be the most taxing on the thermal control system. The thermal scenario of initial deployment is analyzed to determine what temperature the payload boundary conditions need to be kept in an un-powered state to ensure that the payload remains in survival temperature ranges (this scenario represents initial deployment and commissioning where the payload may not be powered).

Specific temperature ranges that the host must maintain during storage, operation,

and commissioning for interior radiative faces and mechanical interfaces are defined based on analysis results are defined in section 3.2.5.

3.2.1 Thermal Desktop FEM Model

A thermal desktop finite element model is created to model and predict the temperatures of the NODE payload. All major components are modeled with representative heat loads as expected on orbit based upon their power usage. Table 3.3 displays the power that each component dissipates when in use. Heaters are also included in the model with expected control regimes implemented. Heaters are located on the EDFA (1.5 W) and on the main plate near the beacon camera (0.75 W). Host boundary conditions are input for each case and are varied to identify the bounding cases that the NODE payload satisfies component operating and survival temperature ranges that are listed in section 2.2. Figure 3-5 shows the FEM created with Thermal Desktop.

Table 3.3: Component power dissipations are determined from electrical power usage.

Component	Power Dissipation Pre-transmit [W]	Power Dissipation Transmit [W]
EDFA	6	6
APD (quantity 3)	0.1	0.1
Beacon Camera	1.4	2.5
TOSA	0	1
Electronics (FPGA and daughter board)	1.5	3
RPi Board	0.5	2
Feedback Laser	0	1

The thermal conductance in W/K between two nodes is calculated using Equation 3.2 where k is the thermal conductivity [w/(m×K)] of the connecting material, A is the cross-sectional area [m^2] of the connection, and L is the length [m] of that connection. When a series of connections with multiple materials of various geometric properties is modeled, the thermal conductance is calculated using Equation 3.3.

$$C = k \times \frac{A}{L} \tag{3.2}$$

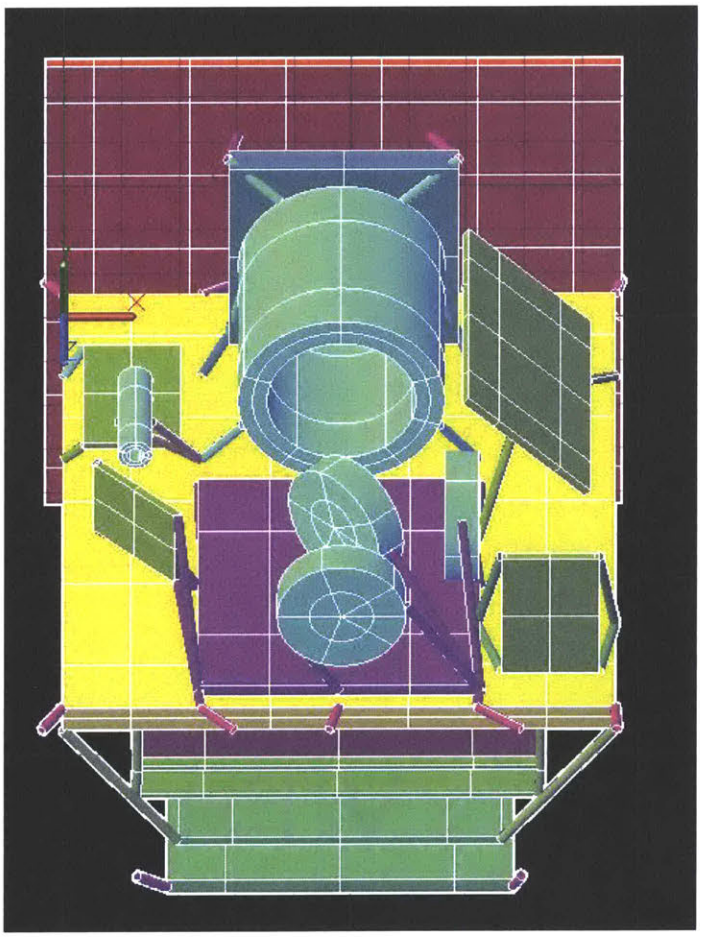

Figure 3-5: Thermal Desktop model of NODE. Mechanical interface with host is not visible but assumed to be mounted with "direct mounting" configuration discussed in section 2.1.6.

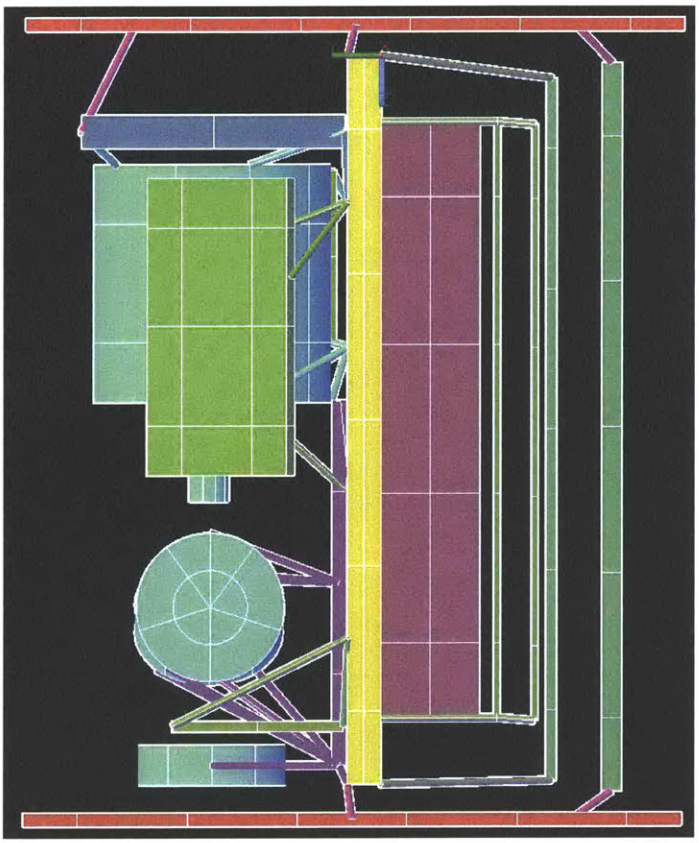

Figure 3-6: Boundary conduction paths are modeled using estimates on TIM joints. Conduction paths can be seen connecting host boundary plates (top and bottom) to NODE payload (center).

$$\frac{1}{C_t} = R_t = R_1 + R_2 + R_3 = \frac{L_1}{k_1 \times A_1} + \frac{L_2}{k_2 \times A_2} + \frac{L_3}{k_3 \times A_3} \tag{3.3}$$

The Thermal Desktop model uses Equations 3.2 and 3.3 to model conductive connections between components including 2216 Berquist TIM connections, standoffs, and mounting structures. Heatflow between the spacecraft and payload occurs primarily at the conductive joints modeled and shown in Figure 3-6. Internal radiation between components and to the interior faces of the spacecraft are also modeled and are the second and final instance of heat flow between the payload and the spacecraft.

Two different TIM are used in the NODE payload. 2216 was chosen as the TIM for a majority of the NODE payload internally (between connections within the payload itself) to simplify assembly. 2216 has a thermal conductivity of 0.4 $\frac{\mathrm{W}}{\mathrm{m}\times\mathrm{K}}$ which is close to (but less than) comparable TIM materials thermal conductivity. While 2216 has

a high CTE, it is not used to mount optical components which could cause them to shatter. 2216 is used to thermally isolate parts and create known thermal connections between components where high thermal conductivity is not necessary.

Bergquist Gap Filler 3500LV is also used as a TIM between standoffs in the electronic stack to increase thermal connectivity of the joints. 3500LV has a high thermal conductivity (3.6 W/k) and is low outgassing. 3500 HV is determined to be necessary as a TIM on the electronics stack to aid heat flow out of the daughter and FPGA electronic boards.

3.2.2 Hot cases

Analysis performed in previous section 2.2.1. indicates that two hot case scenarios will be experienced by the NODE payload. These cases are hot case 1: sunlight operational and hot case 2: sunlight storage .

Both of these scenarios are modeled in Thermal Desktop. During operational scenarios all components are dissipating their maximum expected power for a 15 minute operational period and half power for a 4 minute preparation period before and after operation (for a total of 23 minutes). Actual expected operation time is expected to be less than 9 minutes, therefore there is margin built into modeling results. Spacecraft orientation is not currently considered in the model (the SC would necessarily have to be Earth-pointing to operate the payload) but instead host boundary conditions are directly input as arithmetic nodes. This allows for the determination of host boundary conditions in which temperature range requirements can be met. All structural aluminum components are modeled to have an Alodine finish, all PCBs are assumed to be coated in black paint, and COTS components are modeled with optical properties that are reflective of their exterior coatings. The host interior walls are assumed to be anodized aluminum. Two heaters located on the main plate (0.75 W) and EDFA (1.5 W) are in use during operational scenarios (used to increase component temperatures to operational limits). For storage cases, all components are un-powered and are not dissipating heat, except for the TCS system active components (heaters). Table 3.4 states assumptions made during modeling for each hot

case.

Table 3.4: Assumptions made for each case

Assumption	Hot Operational	Hot Storage
Boundary Conditions	0°C to 25°C	20°C TO 55°C
TCS Powered	Yes	Yes
Component Power Dissipation	Max	None

For the case in which the spacecraft is in full sunlight and operating, all temperatures of components are predicted to remain within their operating temperature ranges. Figure 3-8 displays component survival and operational temperature ranges (dark blue and light blue respectively) and predicted temperature ranges for the hot operational case. For a 23 minute operational case (5 minutes of margin), all components have significant margin except for electronics boards (FPGA and daughter board).The temperature of these boards during TVAC testing will be monitored to ensure that they do not exceed temperature limits for the expected worse case thermal loads on the system. All components maintain their operational temperature requirements seen in section 2.3.

During the modeled hot storage case, all components stay within required operating temperature ranges when the host maintains a maximum temperature of 55°C. As there is no active cooling, the maximum storage boundary conditions are determined in this phase by examining the temperature that components reach and defining boundary conditions so the components to not exceed temperature requirements.

3.2.3 Cold cases

Two cold cases are examined with the Thermal Desktop model. These cases will be cold case 1: eclipse operational and cold case 2: eclipse storage. For both cases, the TCS is active. Table 3.5 compares the different assumptions made in the cold cases examined.

When examining cold case 1 (eclipse operational), it is assumed that the host maintains boundary temperatures between -10°C to 25°C during operation. The thermal model predicts that all temperatures experienced during this case are within

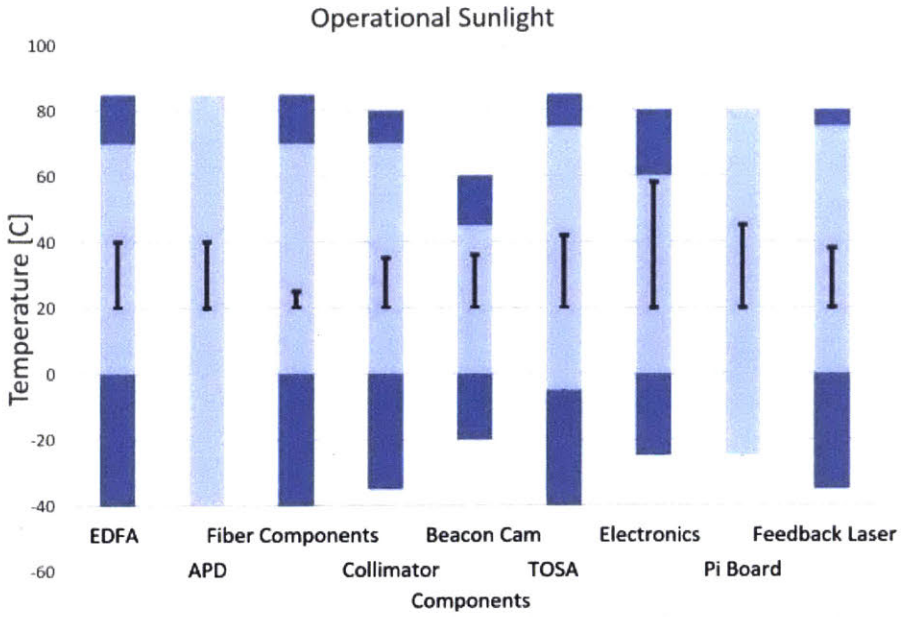

Figure 3-7: Predicted temperatures of components within NODE payload for hot case 1: operational sunlight case. Dark blue bars indicate survival temperature ranges, light blue indicate operational temperature ranges, and black lines indicate predicted temperatures. All components stay within operating temperature ranges.

Table 3.5: Assumptions made for each case

Assumption	Cold Operational	Cold Storage
Boundary Conditions	-10°C to 25°C	-20°C TO 20°C
TCS Powered	Yes	Yes
Component Power Dissipation	Max	None

operational temperature requirements. Predicted temperatures for the scenario are shown in Figure 3-9.

During the cold storage case, NODE boundary conditions are controlled to be within -20°C to 20°C. All internal components within NODE stayed within their survival temperature ranges. Predicted temperatures of components are shown in Figure 3-10.

3.2.4 Commissioning

Payload temperatures are also examined under a commissioning case in which the spacecraft is powered, but the payload is not powered and is not operating its TCS.

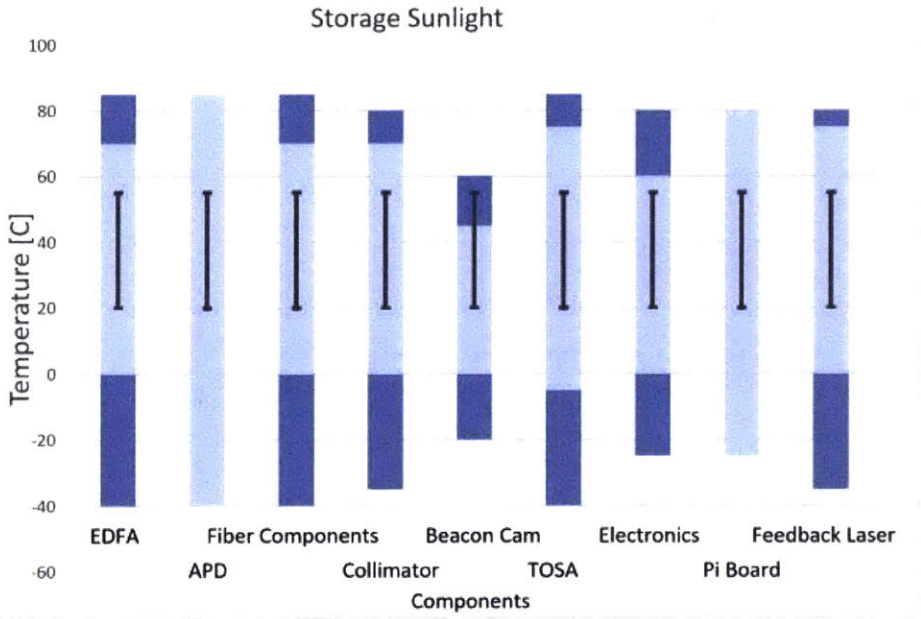

Figure 3-8: Predicted temperatures of components within NODE payload for hot case 2: storage sunlight. Dark Blue bars indicate survival temperature ranges, light blue indicate operational temperature ranges, and black lines indicate predicted temperatures.

This case is meant to simulate the scenario experienced during initial commissioning of the spacecraft. The boundary conditions of the payload are modeled to simulate the periodic eclipse and sunlight loads the spacecraft would experience, however, the spacecraft boundary conditions are controlled to be above -20°C and below 55°C at all times. Predicted temperatures of components are shown in Figure 3-11. All components stay within survival temperatures, but it is worth noting that the host must maintain the payload boundaries between -20°C to 55°C.

3.2.5 Thermal Boundary Requirements

Based on the Thermal Desktop model, it can be determined that the NODE payload will remain within operational and survival temperature ranges for any host that can keep the thermal boundary conditions between -20°C to 55°C when not operating, and -10°C to 25°C when operating. The NODE TCS can be modified to allow for payload operation at a wider range of temperatures if necessary (by adding heater

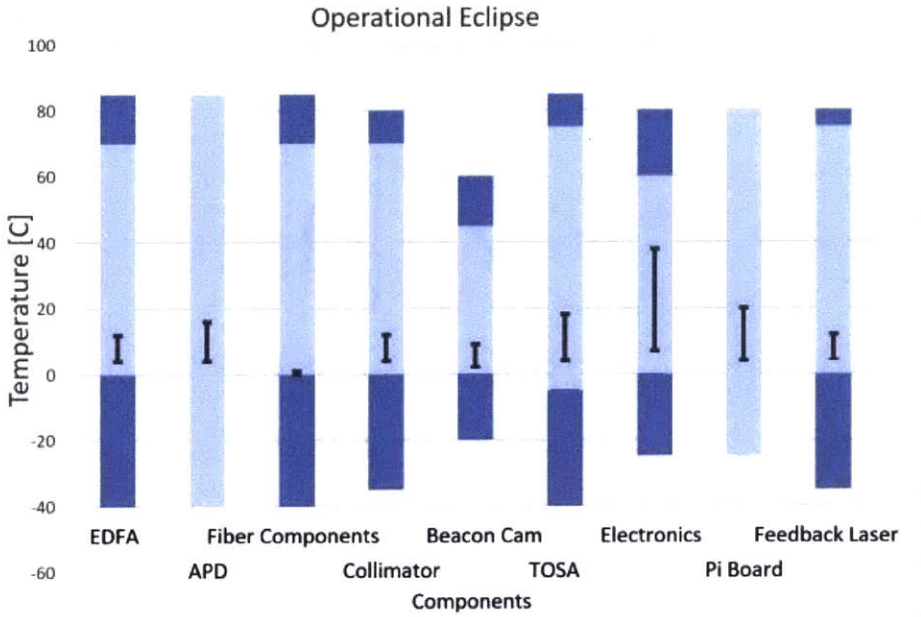

Figure 3-9: Predicted temperatures of components within NODE payload for eclipse (cold) operational case. Dark blue bars indicate survival temperature ranges, light blue indicate operational temperature ranges, and black lines indicate predicted temperatures.

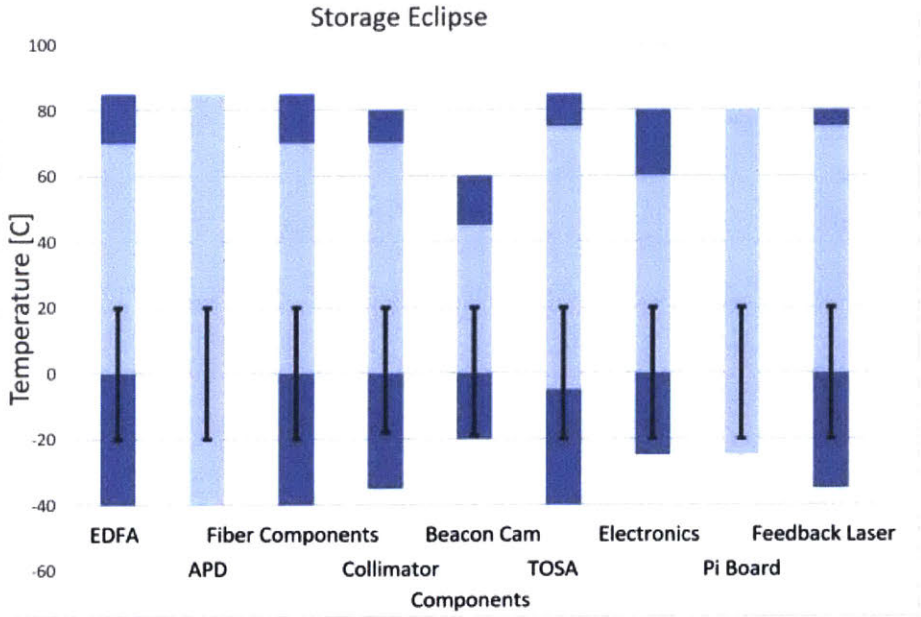

Figure 3-10: Predicted temperatures of components within NODE payload for eclipse (cold) storage case. Dark Blue bars indicate survival temperature ranges, light blue indicate operational temperature ranges, and black lines indicate predicted temperatures.

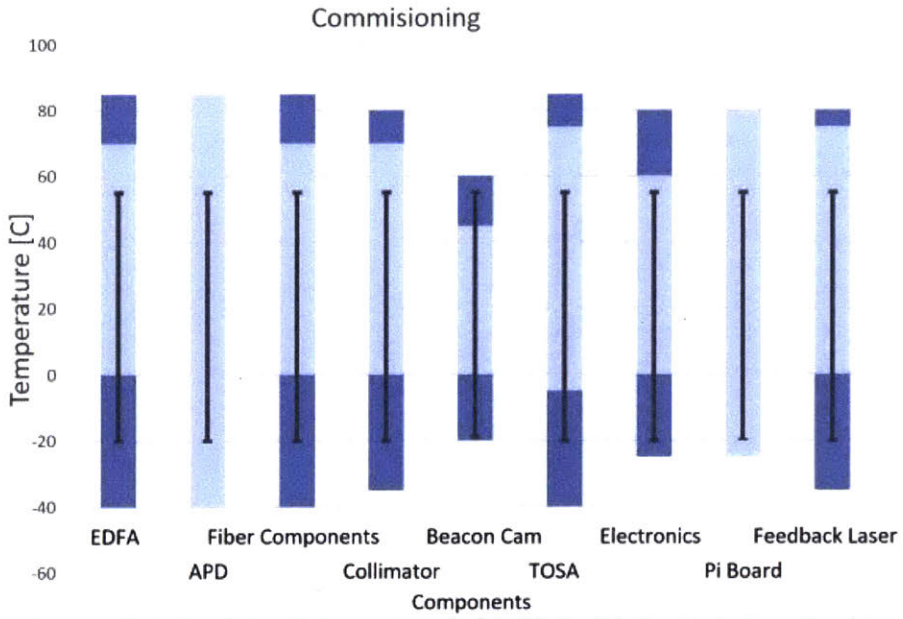

Figure 3-11: Predicted temperatures of components within NODE payload for commissioning case. Dark blue bars indicate survival temperature ranges, light blue indicate operational temperature ranges, and black lines indicate predicted temperatures.

power and changing thermal paths with alternate TIM at Beacon Camera interfaces) without changing mechanical design. When expected host interface temperatures are received, the model should be updated to reflect specific host boundary conditions that may be different. The NODE Thermal Desktop model is available on the MIT Space Systems Laboratory analysis computer and backed up on the MIT STAR Lab NODE repository.

Chapter 4

Structural and Thermal Test Results

A semi-functional prototype is assembled in order to verify that the NODE mechanical and thermal design meets requirements.

At the time of testing, functional PCBs were not available so mass mock-ups are used with a form factor that matched the boards that will be used in flight. Connectors, optical fiber, and wire harnesses were included in the prototype. The prototype is shown in Figure 4-1. The NODE prototype has a mass of 775 g without additional mounting hardware and a mass of 1105 g with the additional mounting hardware. As the PCBs were not functional when assembly began, the prototype is used to verify structural performance through vibration testing but is not used to test thermal performance.

Testing of the TCS is only possible when the PCBs are functional and installed in an Engineering Model (EM) and for that reason TVAC testing is not discussed in this thesis but listed as future work in Chapter 5.

Results of the tests, comparisons to predicted results, and a discussion of the results implications for on-orbit performance are discussed.

4.1 Vibration Testing

Vibration testing is performed on the prototype to determine the first resonant frequency and ensure that there are no structural failures in expected launch environ-

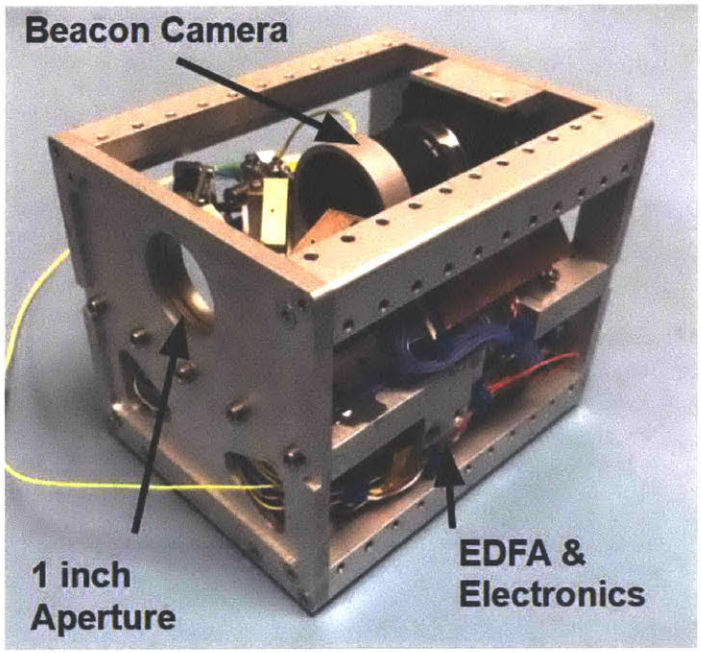

Figure 4-1: Prototype of NODE payload subjected to vibration and thermal cycling testing.

ments. Accelerometers are placed on components that are computationally identified in section 3.1.2 to have low resonant frequencies. Table ?? lists the resonant frequencies of the structure previously predicted in section 3.1.2. A complete table with accelerometer location and orientation (direction in which it measures acceleration) can be found in Table 4.2

Table 4.1: Predicted resonant frequencies of NODE structure, locations, and harmonic.

Order of Resonance	Location	Frequency [Hz]	Harmonic (direction)
1	FPGA Board	500	1
2	Daughter Board	500	1
3	Raspberry Pi Board	700	1
4	FPGA Board	900	2
5	Daughter Board	900	2
-	Coupler Tray	1000	1
-	Coupler Tray	1700	2 (x)
-	Main Plate	2100	1
-	Coupler Tray	2100	2 (z)
-	EDFA	2900	1

The payload is tested to full NASA GEVS qualification levels in order to verify

Table 4.2: Location and orientation of accelerometers during vibration testing

Accelerometer Number	Location	Axis
1	Control (vibration GSE)	Y
2	Pi board	Y
3	FPGA board	Y
4	Camera	X
5	Camera	Y
6	Camera	Z
7	Photodiode board	X/Y
8	FSM Mount	X/Z
9	Dichroic	X/Z
10	Main Plate	Y

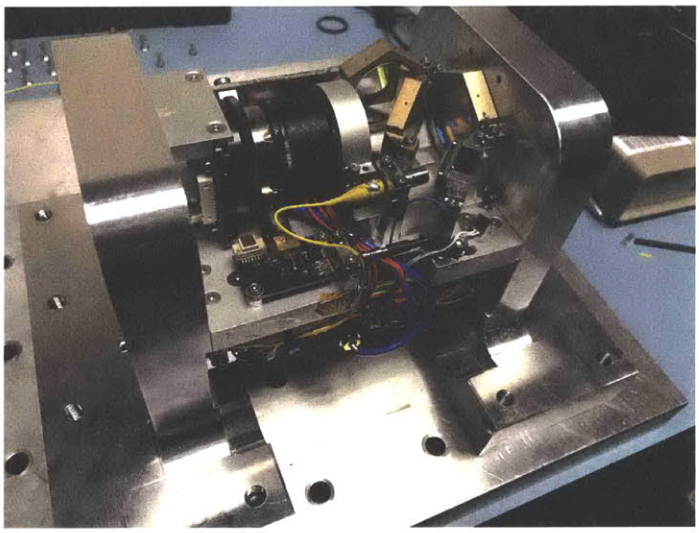

Figure 4-2: NODE payload integrated into vibration fixture.

structural design. The assembly is mounted through the end-plates to the vibration fixture as seen in Figure 4-2. A complete list of the vibration sub-tests and the order in which they were performed can be found in Table 4.3.

After testing is performed, output data from white noise tests is analyzed to identify shifts in the transfer function after random vibe and Sine Burst tests were performed. While the payload experienced small shifts in the first frequency of the system from (shown in Figure 4-3), the shifts are small, indicating it is not the result of structural failure but rather settling of the mechanical system. The first frequency appears to shift from 530 Hz to 520 Hz, which is a shift of 2% and is less than the failure limit of 5% recommended for smalls satellites [11]. Inspection of the mechanical

Table 4.3: List of all vibration test types and order in which they were performed.

Order	Test Type	Axis
1	White Noise	Y
2	Random Vibe	Y
3	White Noise	Y
4	Sine Burst	Y
5	White Noise	Y
6	White Noise	X
7	Random Vibe	X
8	White Noise	X
9	White Noise	Z
10	Random Vibe	Z
11	White Noise	Z

system after testing identified no mechanical failures. A small amount of 2216 was noticed falling from cable harness staking. This staking will not be present in future versions and was used to connect cable connectors to mock-up PCBs. Furthermore, the 2216 that flaked off did not affect joint stiffness.

The accelerometer data is analyzed after the vibrational testing. The first resonant frequency of the NODE structure is determined to be located at the Pi Board and occurs at a frequency of 500 Hz. The structural modeling predicted a first resonant frequency of 500 Hz for the FPGA board as seen in Table 4.1. While the first frequency is not at the component predicted in modeling, it is higher than the 200 Hz design goal discussed in section 2.1.3. Higher order resonances are listed in Table 4.4. Figures 4-4 and 4-5 show the output data of the accelerometers on the Pi and FPGA boards, respectively and are marked to indicate the location of the first and second resonant frequencies. The main plate has a resonant frequency near 1600 Hz which is approximately 20% less than the predicted value of 2000 Hz, but is well over the minimum desired resonant frequency of 200 Hz. A plot of the main plate response can be seen in Figure 4-6.

As discussed in section 2.1.3, the first resonant frequency of the NODE payload must be greater than 200 Hz. Vibration testing indicates that the NODE Payload meets this goal with a first frequency of 500Hz which is above the 200 Hz design goal.

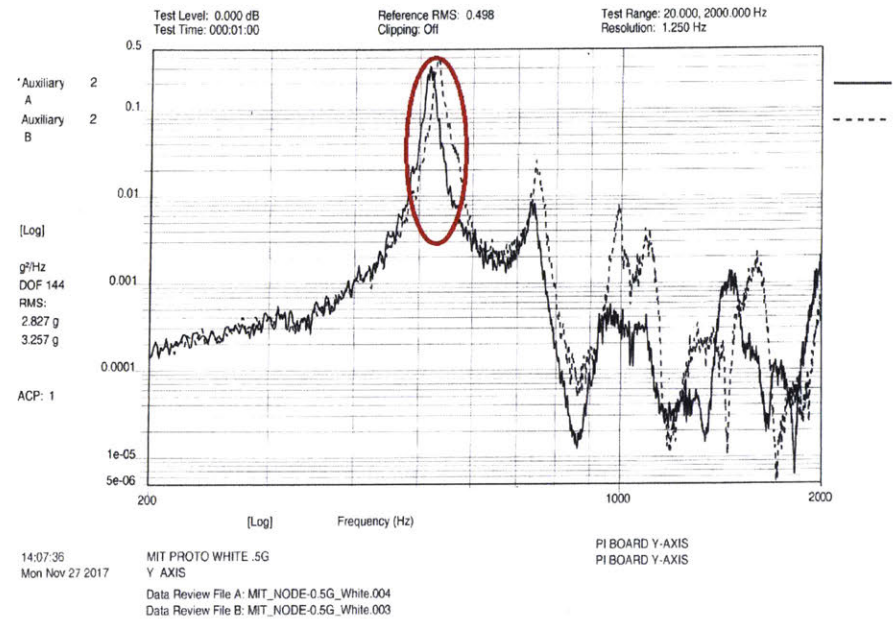

Figure 4-3: Comparison between white noise overlay before and after random vibe in Y axis. Dotted line is before testing and solid line is after. A small shift can be observed in the first frequency location. Shift is less than 5% which is limit for testing failure [11]. First resonant frequency is circled and estimated to be approximately 500 Hz.

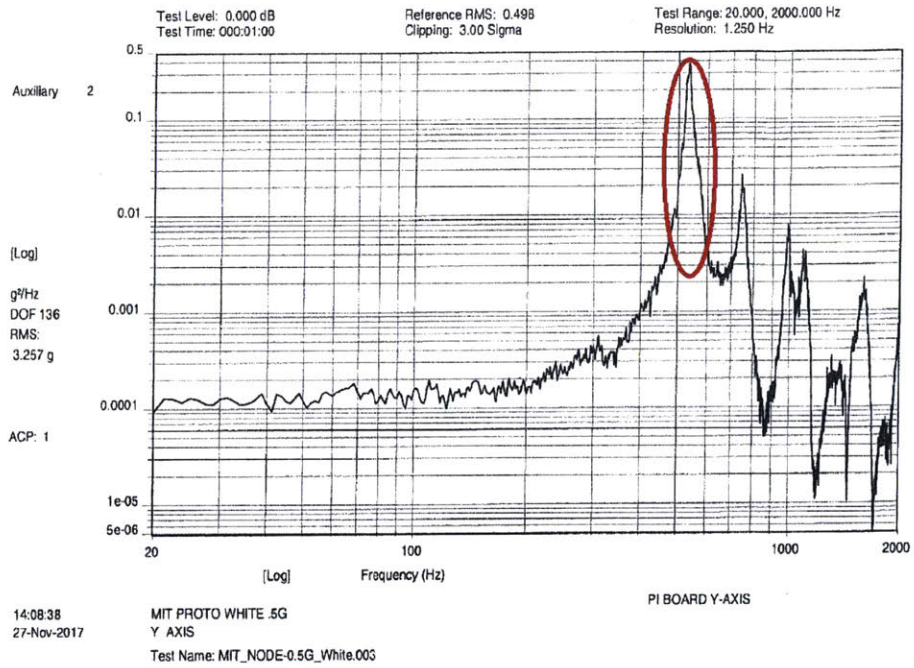

Figure 4-4: Measured system response of accelerometer mounted on Pi Board in Y direction. First resonant frequency is circled and identified to be at 500 Hz.

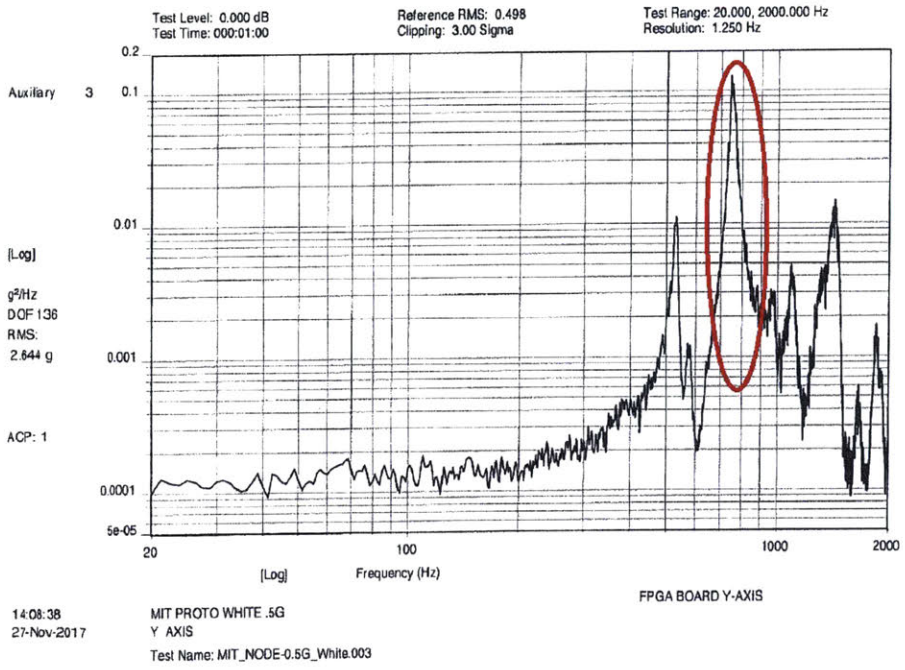

Figure 4-5: Measured system response of accelerometer mounted on FPGA board in Y direction. Second resonant frequency is circled and identified to be at 700 Hz.

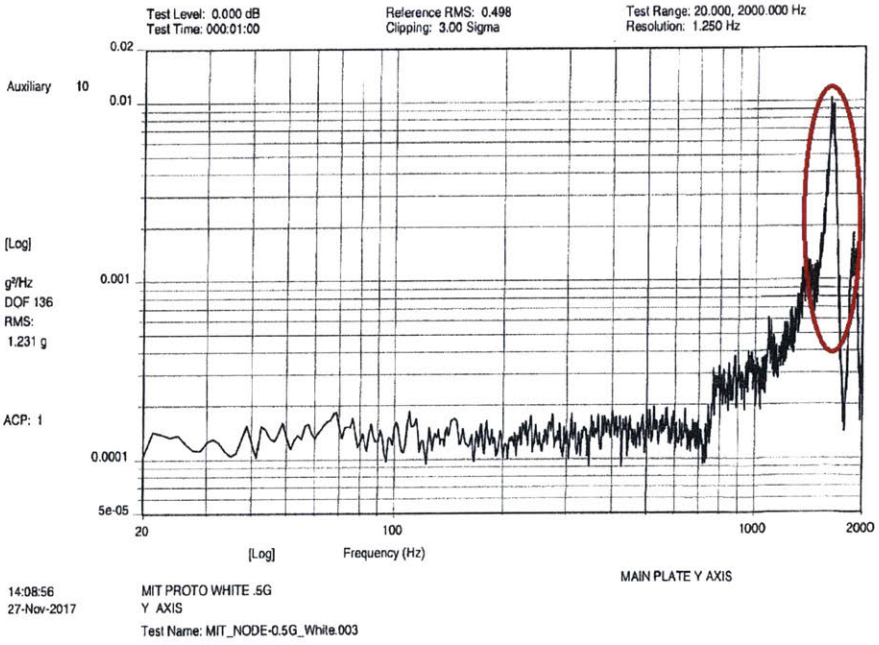

Figure 4-6: Measured system response of accelerometer mounted on main plate in Y direction. Resonant frequency of main structure is circled and identified to be at 1600 Hz.

Table 4.4: Actual resonant frequencies of NODE structure, locations, and harmonic determined during vibration testing.

Order of Resonance	Location	Frequency [Hz]
1	Raspberry Pi Board	500
2	FPGA Board	700
3	Daughter Board	900
-	Coupler Tray	1000
-	Coupler Tray	1500
-	Main Plate	1600
-	Coupler Tray	2100
-	EDFA	2900

4.2 Thermal Testing

Thermal testing has been performed on a component basis but has yet to be performed on a payload level as the currently assembled prototype does not have functional electronics boards. This section discusses TVAC testing of the NODE EDFA, and thermal cycling testing of the FSM.

4.2.1 TVAC Testing

TVAC testing is performed on the EDFA to assess the performance of the component in vacuum under expected environmental loads. The EDFA is not a space-rated component and therefore its performance in vacuum is uncertain. During testing, the EDFA is placed in a vacuum chamber, and operated at expected power levels while the output power and temperature are monitored to evaluate if there are any drops in performance as a function of operating temperature.

The EDFA is thermally isolated from any large thermal masses to simulate a worst-case mounting environment by mounting it on 4 stainless steel standoffs without the use of any TIM. A picture of the TVAC mechanical/thermal interface is shown in Figure 4-7. The EDFA is operated for 15 minutes during each operational cycle and three cycles are performed. The EDFA is operated at 23 dBm (planned power output) for the first cycle, then 24 dBm (maximum power output) for the last two testing cycles. All test cycles start when the EDFA has an average case temperature below

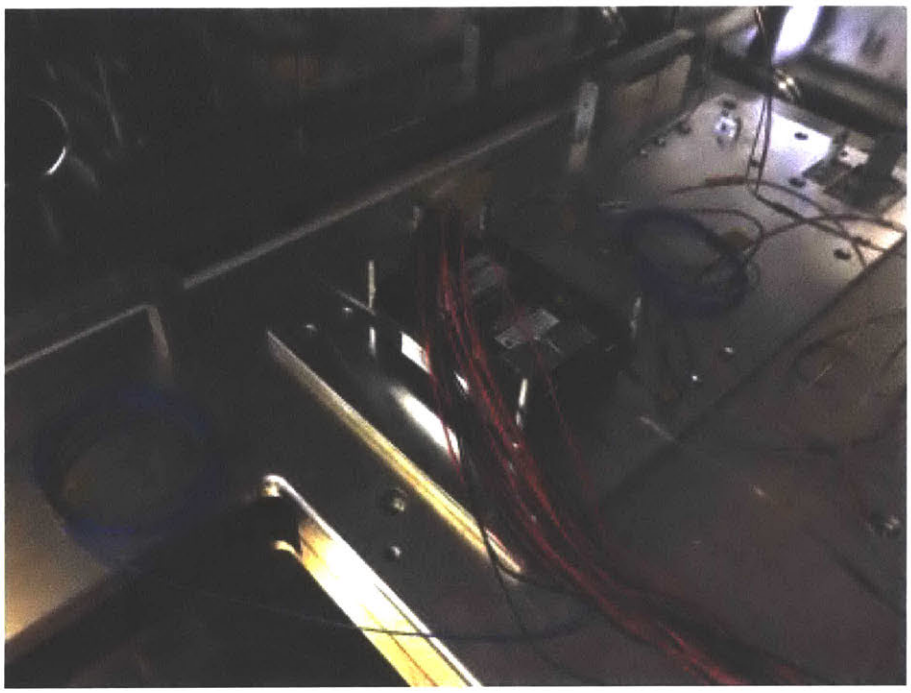

Figure 4-7: EDFA installed into TVAC testing chamber on four stainless steel stand-offs. No TIM is used to minimize the conduction path between the component and plate.

35°C.

During testing, the EDFA reaches a maximum temperature of 55°C which is 10°C below its operational temperature limit of 65°C. When the output power is measured during TVAC testing, it is noted that the EDFA experiences larger output power loss when compared to operating in ambient air. The measured temperatures of the EDFA and output power during the test can be seen in Figure 4-8. Pre-tests and post-tests before TVAC indicate an average loss of 0.2 dBm over the duration of the test while TVAC tests experienced an average of 0.39 dBm loss over the duration of the test. A plot of the output power of the EDFA are shown in Figure 4-9. The EDFA remained functional during testing, and the results of this test are input into link budgets maintained by NODE team members and stored in the MIT STAR Lab NODE repository. While the output power losses are non-negligible, margin held in the link-budget still allows the system to meet 10 Mbps data-rate requirements.

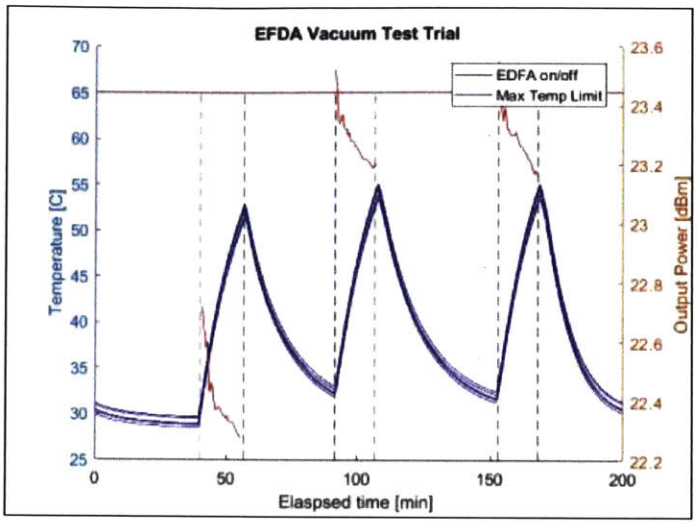

Figure 4-8: Output power and temperature of EDFA plotted over the duration of testing campaign. First cycle EDFA output set to 23 dBm, second and third test cycles set to 24 dBm. EDFA remained within operational temperature requirements during testing. Solid blue lines are temperature measurements from the EDFA, orange lines indicate the output power of the EDFA, black dotted lines indicate operational periods, and the solid red line is the EDFA maximum temperature.

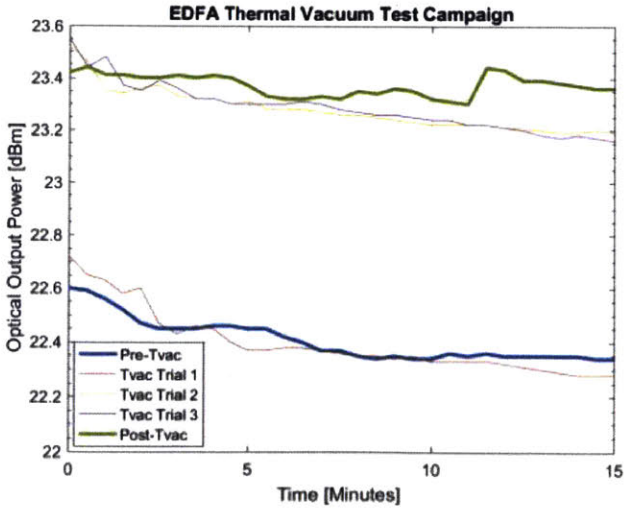

Figure 4-9: Output power of the EDFA during TVAC testing compared to pre/post test results. During TVAC EDFA experienced an average of 0.39 dBm loss compared to 0.2 dBm loss during pre/post testing (in air).

4.2.2 FSM Thermal Cycling

The FSM is also not a space-rated component and its ability to maintain pointing performance over expected temperature ranges is unknown. The FSM was tested in a thermal chamber to assess its performance over expected temperature ranges. Pointing accuracy was measured at each temperature range by using a CMOS detector.

In order to meet system requirements, the FSM must be capable of pointing to within $\pm$ 3.6 arc minutes (or 216 arcseconds) of the commanded location [33]. Test results seen in Figure 4-10 indicate that the FSM can achieve 12 arcsecond (3-σ) pointing accuracy [33]. While this test alone does not prove that the system as a whole meets pointing requirements, it shows that the FSM meets requirements on its performance. Further testing will involve vacuum testing on a system level where pointing performance is verified through operational temperature ranges.

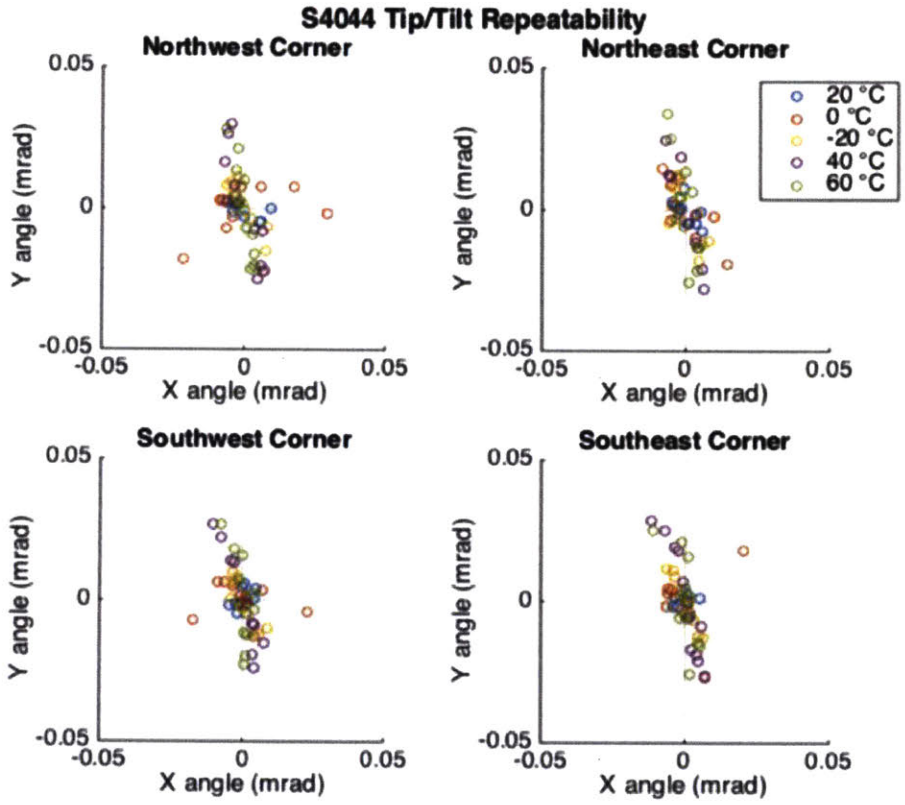

Figure 4-10: Pointing accuracy results of different quadrants of FSM at different temperatures. 3-σ pointing accuracy found to be 12 arcseconds. Requirement is 216 arcseconds (1.05 mrad). [33]

Chapter 5

Conclusion

Results of this thesis are summarized and specific contributions of this thesis are listed. The NODE payload will be completely assembled and ready to integrate with host spacecraft in 2018 and future work required to achieve delivery is discussed.

5.1 Summary

This thesis presents the optomechanical design, analysis, and testing of the Nanosatellite Optical Downlink Experiment (NODE). NODE aims to deliver a 10-100 Mbps downlink in a CubeSat form factor.

Expected environmental loads are examined and an optic mounting scheme where optics are mounted to bezels with RTV 566 is developed. Expected launch loads of the adhesive bonds are analyzed and optical bond failure is not predicted to occur with a margin of safety of 11. The first resonant frequency of the main structural plate is estimated to be 2000 Hz, and fastener margins of safety for shear, tension, and separation are all calculated to be greater than 200 for the largest optical element. Thermoelastic fastener stresses were not considered in this thesis as safety margins are large, but are listed as future work in section 5.3. Depressurization analysis is performed assuming a 1 mm $\times$ 1 mm venting hole, and a maximum pressure differential of 7000 Pa is calculated. Pressure loading that could occur on optical bonds are added to gravity loading and optical bond shear margin of safety is calculated to

be 6.

Component operational and survival temperature ranges are examined and worst case operational and storage thermal cases are predicted using a one node thermal model. The beacon camera component has the narrowest allowable temperature range (0°C to 45°C when operating, and -20°C to 60°C when in storage). The one node model predicts temperatures ranging from -40°C to 100°C which will exceed component temperature requirements without a TCS. A preliminary NODE TCS is presented that consists of two heaters (0.75 W on the main plate near the camera, and 1.5 W on the EDFA), TIM, and Alodine surface coatings to maintain components within allowable operational temperatures. Four bounding operational and storage cases (sunlight operational, sunlight storage, eclipse operational, and eclipse storage) are identified for later thermal analysis.

Computational structural and thermal modeling and analysis and performed for the NODE payload. The first resonant frequency of the NODE payload is predicted to be at 500 Hz at the RPi board and the resonant frequency of the main plate is predicted to be at 2100 Hz. The hand calculations and the computational model results match to within 5%. Static loading analysis is performed with loads of 20g and a margin of safety of greater than 5 is met for all axes.

Thermal analysis is performed in Thermal Desktop for 5 identified thermal bounding cases and component operational and survival temperatures. For all cases, all component temperatures are maintained between 0°C and 60°C when operating, and -20°C to 55°C which are within allowable flight temperatures. Host thermal interface conditions are expected to be maintained at ranges of -10C to 25C when operating, and -10 to 55C when in storage mode. When a specific host is identified, analysis should be updated to reflect and changes in thermal interface. NODE interface temperature requirements listed above could be expanded with the addition of more powerful heaters. If it is deemed necessary to expand the thermal interface temperature range, analysis should be performed to identify required heater power ranges and is listed as future work in section 5.3.

A mechanical prototype of the NODE payload is developed and tested. Vibration

testing results indicate that the first resonant frequency of the node structure is 500 Hz, and while small shifts in the system were experienced during testing, they are less than the failure criteria ??. Analysis and simulation both predict a first resonant frequency of 500 Hz.

Component level TVAC tests on the EDFA are performed, and a 0.2 dBm loss is measured when operating in TVAC. Functional performance in vacuum is verified in a worst-case thermal environment and losses do not prevent NODE system from meeting 10 Mbps data rate goals. Previous thermal cycling testing results of the FSM are discussed.

5.2 Thesis Contributions

Specific contributions of this thesis include:

- Structural design of the NODE optical communications terminal that meets mission requirements
- Development of a thermal control system capable of meeting system requirements onboard a variety of host spacecraft
- Structural analysis indicating positive margins of safety for expected environmental loading.
- Thermal Analysis showing that TCS meets mission requirements in all operational phases.
- Prototype mechanical and thermal testing results for the NODE payload.

5.3 Future Work

Required work moving toward a delivered payload include:

- Electronics Flat-sat integration and testing to verify software and electronics design. Electronics need to be fully tested on a component level and when integrated together to verify functionality.

- Final Integration of EM and FM units. EM and FM units are currently midway though integration but are waiting on complete and tested electronics boards to proceed.

- Functional software and system testing of NODE payload. After the EM and FM are assembled, functional tests should be performed with the units to verify functionality of software,electronics, and internal payload interfaces.

- Lab "over-the-air" testing where completed EM transmits data to ground station and demodulation is performed.

- Thermal Vacuum testing of NODE payload to verify TCS performance.

- Thermal Vacuum testing of NODE payload to verify system performance (measure metrics such as data transmitted, pointing performance, etc).

- Qualification level vibration testing on NODE EM to verify structural design.

- Acceptance level vibration testing on NODE FM to screen for workmanship errors.

- Identification of NODE Host spacecraft and interfaces with Host SC.

- Updated thermal and structural analysis if host boundary conditions are different than that examined in this thesis

- High fidelity thermal and structural analysis including PCB component masses and host spacecraft Thermal Desktop model if required by host or LSP

- Mechanical Fit-check with Host spacecraft.

- Software/Data interface testing with Host spacecraft.

- NDOE integration with Host spacecraft.
- Host SC vibration testing.
- Host SC TVAC testing.
- Deployment of ground station.
- Host SC delivery to Launch Service Provider

Appendix A

Calculations/Code

```
 % Derek Barnes
close all
clear all

%% preload claulation, Nasa tech memorandum 106943
T = 0.3; %N-m torque applied, gets us to 75% of maximum
    preload.
K = .15; % nut factor, 1.5 conservative estimate for
    separation analysis. Nasa tech memorandum 106943
D = .002; % nominal diameter, m2

u = .25; %uncertainty on applied preload using torque
    wrench, according to Nasa tech memorandum 106943
P_o_min = T/(K*D)*(1-u) % N
P_o_max = T/(K*D)*(1+u) % N

%% Joint stiffness, Nasa tech memorandum 106943

E = 6.9e10; %Pa, youngs modulus of material
d = .002; %shaft area
alpha = 30;%deg
D = .0038; %head area
t = .004; %m, thread distance
```

```
p1 = 3.14 * E * d * tand(alpha);
p2 = (2*t*tand(alpha) + D - d)*(D + d);
p3 = (2*t*tand(alpha) + D + d)*(D - d);
stiffness_joint = p1/log(p2/p3);

%% Joint stiffness , Nasa tech memorandum 106943
A = pi*(d/2)^2; % area of screw shaft
E_b = 1.93e11 ; % Pa stainless steel 304
L = .008; %m - 8mm screw

k_b = A * E_b /L; % bolt stiffness

stiffness_factor = k_b/(k_b+stiffness_joint)
%% separation margin of safety, Nasa tech memorandum 106943
n = .75;

% calulate External force on screws
m_body = .033; %kg
num_gs = 20;
num_fasteners = 2;
gravity_constant = 9.8; %m/s^2
%free body diagram, f = ma where external forces are gravity
   and fastener
%joint force
% mg(20) - 2*p_ext = ma      ; assuming 20gs of acceleration
%ma = 0 since we are assuming the joint is holding
%P_ext = mg*10
%g = 9.8 m/s^2
%m = 26g + 7g =  .033kg
P_external = gravity_constant * num_gs/num_fasteners*m_body

P_sep = (1-n*stiffness_factor) * P_external

SF_sep = 1.25; % safety factor separation, 1.2 recommended
   for structural applications , Nasa tech memorandum 106943
MS_sep = P_o_min / (SF_sep * P_sep) - 1

%% shear margin screws  Nasa tech memorandum 106943
D = .002% [m] nominal shaft area
p =.0004;% thread pitch in m
A_s = 3.14 /4 * (D-.09743*p)^2;
F_su = 5e8; %pa
shear_allow = F_su * A_s;
%Free body diagram
%f = ma where external forces are gravity and fastener joint
```

```
    force
%mg(20) - 2*V = ma , assuming not moving so a = 0
% mg(10) = V
V = gravity_constant*num_gs/num_fasteners*m_body; % newtons
    of force
SF_shear = 1.25;

MS_shear = shear_allow/ (SF_shear*V) - 1
%% tension margin screws  Nasa tech memorandum 106943
%Free body diagram
%f = ma where external forces are gravity and fastener joint
    force
%mg(20) - 2*p_b = ma , assuming not moving so a = 0
% mg(10) = p_b

p_b = gravity_constant*num_gs/num_fasteners*m_body ; % total
    axial bolt load [n]
F_ty = 4.62e8; % tensile yeild strength
F_tu = 8e8; %tensile ultimate strength

tensile_allow = F_ty * A_s;
MS_tension =  tensile_allow / (p_b) - 1

%% combined tension and shear

%% venting calculation Spacecraft com,partment venting, John
    J Scialdone
g = 9.8;%m/s^2
R = 29.2; %m/K
T = 298; %k, assumed
V =.110*.096*.096 ;%m^3 %volume of cavity
A_orifice = .001*.001;%m^2 %area of orifice leaking air
C_orifice_discharge = .65;% orifice discarge coefficient

t_end = 110; %sec

t_fit_dpdt = [0:10:t_end];
dp_dt_fit_dt_dt = 6894.76*[0 .15 .25 .35 .75 .55 .25 .2 .15
    .1 .05 .02 ]; % %pa
t_fit_dpdt2 = [0:5:t_end];
dp_dt_fit_dt_dt2 = 6894.76*[0 .15 .25 .35 .75 .55 .25 .2 .15
    .1 .05 .02 .02/2 .02/4 .02/8 .02/16 .02/32 .02/64 .02/128
    .02/256 .02/512 .02/1024 .02/2048];

t = [0:1:t_end];
```

```
P_int = 101325 * ones(1,length(t));

Adjustment_factor = 1.03; % to fix offset from 0 pressure

dp_dt_ext2 = interp1(t_fit_dpdt2,dp_dt_fit_dt_dt2,t)*
   Adjustment_factor;

figure;
hold on
plot(t,dp_dt_ext2,'b')
xlabel('Time [s]')
ylabel('dP/dt [Pa/s]')

P_o_ext = 101325 * ones(1,length(t));

for ii=2:length(t)
    P_o_ext(ii) =  P_o_ext(ii-1) -  dp_dt_ext2(ii);

end

figure;
hold on
plot(t,P_o_ext,'b');
xlabel('Time[s]');
ylabel('Pressure External [Pa]');

delta_p_int = zeros(1,length(t));
for ij=2:length(t)

p1 = 1/(2*g*R*T);
p2 = (V/(A_orifice*C_orifice_discharge))^2;
p3 = (dp_dt_ext2(ij))^2;
p1*p2*p3/P_o_ext(ij);
delta_p_int(ij) = p1*p2*p3./P_o_ext(ij);

P_int(ij) = P_o_ext(ij)-delta_p_int(ij);

end

hold on
xlabel('Time [s]')
ylabel('Pressure [Pa]');
plot(t,P_int,'r');
legend('Fairing Pressure','Payload Pressure');
```

```
title('Payload and Fairing Pressure vs Time');
axis([0 60 0 101325])

figure
hold on
title('Pressure Difference vs Time (Payload Interior -
   Fairing)')
xlabel('Time [s]')
ylabel('Pressure difference [Pa]');
plot(t,delta_p_int,'r');
axis([0 60 0 7500])
%% Stress experienced by optic bond due to gravity loads
 n_bonds = 6;
 A_optic_bond = 7e-6; %m^2
 g = 9.8; % m/s^2
 num_gs = 20;
 m_optic = .026; %kg
 shear_yield_RTV = 3.24e6; %Pa

G_y_grav = m_optic *g*num_gs /(n_bonds*A_optic_bond)

FS_6bonds_grav = shear_yield_RTV/G_y_grav

G_y_grav_3bonds = m_optic *g*num_gs /(n_bonds/2*A_optic_bond)

FS_3bonds_grav = shear_yield_RTV/G_y_grav_3bonds

%% stress experienced by optic bond due to pressure
   differential
  shear_yield_RTV = 3.24e6; %Pa
 delta_P_max = 7000; %Pa
 n_bonds = 6;
 area_optic =.000486;
 F_p = area_optic * delta_P_max;
 F_optic_bond = F_p;
 A_optic_bond = 7e-6; %m^2

 G_y_press_6bonds = F_optic_bond/(A_optic_bond * n_bonds)

 FS_6bonds_press_grav
    =shear_yield_RTV/(G_y_grav+G_y_press_6bonds)

 G_y_press_3bonds = F_optic_bond/(A_optic_bond * n_bonds/2)

 FS_3bonds_press_grav
```

```
   =shear_yield_RTV/(G_y_grav_3bonds+G_y_press_3bonds)

%% Thermal equalibrium temps for 1 node model
%{
hot case:
assuming that spacecraft is facing earth and operating or
   is generating
solar heat in a standby case with max exposed area to sun.
cold case:
during eclipse with a 1u face pointing nadir to minimize
   planetshine and
operational or
during eclipse with storage no payload power but max
   exposed area to
earth.
%}

% hot case
Power_safety_margin = 1.2;
J_s = 1367;%W/m^2
A_panel = 4 * .1 * .3; %area of 4 solar panels
A_3U_side = .3*.1;
A_1U_side = .1*.1;

orbit_altitude = 500000;%m (500 km)
R_earth = 6.371e6;
M_earth = 5.98e24; %kg
G = 6.673e-11;%Nm^2/kg^2
albedo_factor = .3; % earth, high estimate for max temp
orbit_peroid = sqrt( (4*pi^2 * (R_earth +orbit_altitude)
   ^3)/(G * M_earth));
eclipse_portion =  2 * asind(R_earth /(R_earth
   +orbit_altitude)) /360;
time_eclipse = orbit_peroid * eclipse_portion; % s

solar_cell_eff = .2;
packing_eff = .85;
converter_eff =.8;
P_generated_est_per_orbit = A_panel * J_s * solar_cell_eff
   * packing_eff * converter_eff * (1-eclipse_portion);

absorb_solarcell = .8; % double deployable
emiss_solarcell = .8;

absorb_3U_faces = .08;  % alodined coating
```

```
emiss_3U_faces = .15;

absorb_1U_faces = .08;  %
emiss_1U_faces = .15;

boltzman_constant = 5.67*10^(-8); %[W/m^2 K^4]
VF_albedo = 1.4 ; %estimate from fortescue



%% Hot case op and storage

%operational, nadir pointing 15W payload + 30W SC + 20%
    margin

Q_sc = 20 *Power_safety_margin;%W
Q_p = 15* Power_safety_margin;%W

Q_in_solar_op =   J_s*absorb_1U_faces * A_1U_side;

Q_in_albedo_op = J_s *albedo_factor * VF_albedo*(
    absorb_1U_faces * A_1U_side);

Q_in_ps_op = 237* (R_earth/(R_earth +orbit_altitude))^2 *(
    emiss_1U_faces * A_1U_side);

T_sun_op_C= ((Q_sc + Q_p + Q_in_solar_op + Q_in_albedo_op +
    Q_in_ps_op)/...
      ( boltzman_constant*(emiss_solarcell*A_panel*2 +
         4*A_3U_side*emiss_3U_faces +
         2*emiss_1U_faces*A_1U_side   ) ) )^(1/4) -273.15

%storage

Q_sc = 20 *Power_safety_margin;%W
Q_p = 0;%W


Q_in_solar_stor =   J_s*absorb_3U_faces * A_3U_side + J_s
    *absorb_solarcell*A_panel ;

Q_in_albedo_stor = J_s *albedo_factor * VF_albedo*(
    absorb_3U_faces * A_3U_side + absorb_solarcell*A_panel);

Q_in_ps_stor = 237* (R_earth/(R_earth +orbit_altitude))^2
```

```
    *( emiss_3U_faces * A_3U_side + emiss_solarcell*A_panel);

T_sun_stor_C= ((Q_sc + Q_p + Q_in_solar_stor +
    Q_in_albedo_stor + Q_in_ps_stor)/...
     ( boltzman_constant*(emiss_solarcell*A_panel*2 +
        4*A_3U_side*emiss_3U_faces +
        2*emiss_1U_faces*A_1U_side   ) ) )^(1/4) -273.15


%% Eclipse Operational and storage temps

% exposing max area to earth
Q_sc_ecl_stor = 20; %W
Q_p_ecl_stor = 0 ;%W
Q_in_ps_ecl_stor =237* (R_earth/(R_earth
    +orbit_altitude))^2 *( emiss_solarcell * A_panel +
    emiss_3U_faces * A_3U_side); %assuming that only a 1u
    face is pointing to earth for min energy in

T_ecl_stor_C= ((Q_sc_ecl_stor + Q_p_ecl_stor +
    Q_in_ps_ecl_stor)/...
     ( boltzman_constant*(emiss_solarcell*A_panel*2 +
        4*A_3U_side*emiss_3U_faces +
        2*emiss_1U_faces*A_1U_side   ) ) )^(1/4) -273.15

% ecl op

% nadir pointing
Q_sc_ecl_op = 20; %W
Q_p_ecl_op = 15 ;%W
Q_heaters_op = 0;%W
Q_in_ps_ecl_op =237* (R_earth/(R_earth +orbit_altitude))^2
    *( emiss_1U_faces * A_1U_side); %assuming that only a 1u
    face is pointing to earth for min energy in

T_ecl_op_C= ((Q_heaters_op+Q_sc_ecl_op + Q_p_ecl_op +
    Q_in_ps_ecl_op)/...
     ( boltzman_constant*(emiss_solarcell*A_panel*2 +
        4*A_3U_side*emiss_3U_faces +
        2*emiss_1U_faces*A_1U_side   ) ) )^(1/4) -273.15



%% Hot case op and storage
```

```
%operational, nadir pointing 15W payload + 30W SC + 20%
    margin

Q_sc = 20 *Power_safety_margin;%W
Q_p = 15* Power_safety_margin;%W

Q_in_solar_op =    J_s*absorb_1U_faces * A_1U_side;

Q_in_albedo_op = J_s *albedo_factor * VF_albedo*(
   absorb_1U_faces * A_1U_side);

Q_in_ps_op = 237* (R_earth/(R_earth +orbit_altitude))^2 *(
    emiss_1U_faces * A_1U_side);

T_sun_op_C= ((Q_sc + Q_p + Q_in_solar_op + Q_in_albedo_op +
    Q_in_ps_op)/...
     ( boltzman_constant*(emiss_solarcell*A_panel*2 +
        4*A_3U_side*emiss_3U_faces +
        2*emiss_1U_faces*A_1U_side   ) ) )^(1/4) -273.15

%storage

A_3U_side_45 = A_3U_side*cosd(45);

Q_sc = 20 *Power_safety_margin;%W
Q_p = 0;%W


Q_in_solar_stor = J_s*absorb_3U_faces * A_3U_side_45 + J_s
    *absorb_solarcell*A_panel ;

Q_in_albedo_stor = J_s *albedo_factor * VF_albedo*(
    absorb_3U_faces * A_3U_side_45 +
    absorb_solarcell*A_panel);

Q_in_ps_stor = 237* (R_earth/(R_earth +orbit_altitude))^2
    *( emiss_3U_faces * A_3U_side_45 +
    emiss_solarcell*A_panel);

T_sun_stor_C= ((Q_sc + Q_p + Q_in_solar_stor +
    Q_in_albedo_stor + Q_in_ps_stor)/...
     ( boltzman_constant*(emiss_solarcell*A_panel*2 +
        4*A_3U_side*emiss_3U_faces +
        2*emiss_1U_faces*A_1U_side   ) ) )^(1/4) -273.15
```

```
%% CTE calc
%Tilt
D2 = .038;
D1 = .010;
D_m = .038;

delta_T2 = 5;
delta_T1 = -5;

CTE_al = 24/1000000;

delta_D2 = D2 * delta_T2 * CTE_al;
delta_D1 = D1 * delta_T1 * CTE_al;

delta_D2_mm = delta_D2 * 1000;
delta_D1_mm = delta_D1 * 1000;

D2_new = D2 + delta_D2;
D1_new = D1 + delta_D1;

D_top =D2_new - D1_new;
before =atan((D2-D1)/D_m);

theta_misalign = abs(atan((D2 + delta_D2 - (D1 +
   delta_D1))/D_m) - before)
theta_misalign_mrad = theta_misalign*1000

%% tip

h_post = .02;
d_across = .005;
delta_D1 = 1;

delta_D1 = h_post * CTE_al *delta_D1;
delta_D2 = h_post * CTE_al *-1*delta_D1;

theta_tip = atan((delta_D1 + delta_D2)/d_across)*1000
```

Bibliography

[1] Robert C. Baumann. *General Environmental Verification Specification for STS and ELV Payloads, Subsystems, and Components.* NASA GODDARD SPACE FLIGHT CENTER, Greenbelt, Maryland 20771, rev a edition, June 1996. NASA GEVs.

[2] Nacer E. Chahat. New antennas will take cubesats to mars and beyond. https://spectrum.ieee.org/aerospace/satellites/new-antennas-will-take-cubesats-to-mars-and-beyond, 2018. Accessed: 2018-5-16.

[3] Jeffery A. Chambers. Preloaded joint analysis methodlogy for space flight systems, December 1995. NASA Technical Memorandum 106943.

[4] Michael Chrisp. Optical design of the camera for transiting exoplanet survey satellite (tess). https://ntrs.nasa.gov/archive/nasa/casi.ntrs.nasa.gov/20150018419.pdf. Accessed: 2018-5-18.

[5] Andrew Clements. Selection of optical adhesives. https://wp.optics.arizona.edu/optomech/wp-content/uploads/sites/53/2016/10/ClementsTutorial1.doc. Accessed: 2018-2-14.

[6] Emily Clements. Nanosatellite optical downlink experiment: Design, simulation, and prototyping. https://www.spiedigitallibrary.org/journals/Optical-Engineering/volume-55/issue-11/111610/Nanosatellite-optical-downlink-experiment-design-simulation-and-prototyping/. Accessed: 2018-5-16.

[7] Bernard L. Edwards et. all. Overview of the laser communications relay demonstration project, 2012.

[8] Darren Rowen et. all. Ocsd-a / aerocube-7a status update. http://mstl.atl.calpoly.edu/ bklofas/Presentations/DevelopersWorkshop2016/, April 2016. Accessed: 2018-2-7.

[9] Hyosang Yoon et. all. Satellite tracking system using amatuer telescope and star camera for portable optical ground station. Conference on Small Satellites -30th Annual AIAA/USU.

[10] Tam Nguyen et. all. Development of a pointing, acquisition, and tracking system for a cubesat optical communication module. https://www.spiedigitallibrary.org/conference-proceedings-of-spie/9354/1/Development-of-a-pointing-acquisition-and-tracking-system-for-a/10.1117/12.2080591.short?SSO=1.

[11] Tom Sarafin et. all. Vibration testing of small satellites - part 3. http://www.instarengineering.com. Accessed: 2018-5-20.

[12] FCC. Fcc authorizes spacex to provide broadband satellite services. https://www.fcc.gov/document/fcc-authorizes-spacex-provide-broadband-satellite-services. Accessed: 2018-5-16.

[13] FCC. Fcc fact sheet* streamlining licensing procedures for small satellites. notice of proposed rulemaking, ib docket no. 18-86. https://transition.fcc.gov/, 2018. Accessed: 2018-5-15.

[14] Tony Greicius. Psyche overview. https://www.nasa.gov/missionpages/psyche/overview/index.html, September 2017. Accessed: 2018-1-26.

[15] Caleb Henry. Fcc issues warning in wake of swarm's unauthorized launch. http://spacenews.com/fcc-issues-warning-in-wake-of-swarms-unauthorized-launch/, 2018. Accessed: 2018-5-15.

[16] ASM Aerosapce Specification Materials Inc. Aluminum 6061-t6; 6061-t651. http://asm.matweb.com/search/SpecificMaterial.asp?bassnum=ma6061t6.

[17] Sinclair Interplanetary. Optical communications. http://www.sinclairinterplanetary.com/opticalcomms, Al 26. Accessed: 2018-2-7.

[18] Paul Yoder Jr. Optomechanical design in five easy lessons. http://spie.org/newsroom/optomechanical-design-in-five-easy-lessons, 2004. Accessed: 2018-5-15.

[19] Ryan W. Kingsbury. Optical communications for small satellites, 2015.

[20] Bryan Klofas. 88 satellite deployment and frequency licensing for planet's earth imaging constellation. http://mstl.atl.calpoly.edu/ bklofas/Presentations/DevelopersWorkshop2017, dec 2015. Accessed: 2018-5-16.

[21] Erik Kulu. Nanosatellite database. http://www.nanosats.eu/index.html, April 2018. Accessed: 2018-4-5.

[22] MIT Lincoln Laboratory. Professional society fellows - don m boroson. https://www.ll.mit.edu/about/bios/boroson-d.html. Accessed: 2018-5-16, one of few references of GeoLITE.

[23] Proto Labs. Design guidelines: Cnc milling. https://www.protolabs.com/services/cnc-machining/cnc-milling/design-guidelines/. Accessed: 2018-2-13.

[24] Thor Labs. 1550 nm pigtailed aspheric collimators - cfs5-1550-apc. https://www.thorlabs.com/. Accessed: 2018-5-19.

[25] Roland Lagier. *Ariana 5 User's Manual.* Arianespace, Greenbelt, Maryland 20771, issue 5 revision 2 edition, October 2016.

[26] Myron Lee. Optomechanical and wavelength alignments of cubesat laser communication systems, 2017.

[27] Thuy Mai. Benefits of optical communications. https://www.nasa.gov/directorates/heo/scan/engineering/technology/, May 2016. Accessed: 2018-1-26.

[28] Doug Messier. Nasa laser system sets record with data transmissions from moon. http://www.parabolicarc.com/2013/10/22/nasa-laser-system-sets-record-data-transmissions-moon/, October 2013. Accessed: 2018-1-26.

[29] Tam Thuc Nguyen. Laser beacon tracking for free-space optical communication on small-satellite platforms in low-earth orbit. https://dspace.mit.edu/bitstream/handle/1721.1/101446/939660395-MIT.pdf?sequence=1, 2013. Accessed: 2018-5-16.

[30] Gunter's Space Page. Hodoyoshi 2 (risesat). http://space.skyrocket.de/. Accessed: 2018-5-16.

[31] Chris Peat. Iss - orbit. https://heavens-above.com/orbit.aspx?satid=25544. Accessed: 2018-5-18.

[32] Earth Observation Portal. Edrs (european data relay satellite) constellation / spacedatahighway. https://directory.eoportal.org/web/eoportal/satellite-missions/e/edrs, November 2008. Accessed: 2018-1-26.

[33] Kathleen Michelle Riesing. Development of a pointing, acquisition, and tracking system for a nanosatellite laser communications module, 2015.

[34] Kathleen Michelle Riesing. Portable optical ground stations for satellite communication, 2018.

[35] Satnews. Nanoracks completes fourth external cargo ship satellite deployment mission, largest to date. http://www.satnews.com/story.php?number=352166275, December 2017. Accessed: 2018-2-7.

[36] Andreas Schutz. Dlr communicates with terrasar-x earth observation satellite via laser beam. http://www.dlr.de/en/desktopdefault.aspx, November 2008. Accessed: 2018-1-26.

[37] Katie Schwertz. Useful estimations and rules of thumb for optomechanics. Technical Report, May 2010.

[38] John J.. Scialdone. Spacecraft compatment venting. https://ntrs.nasa.gov/archive/nasa/casi.ntrs.nasa.gov/19980236692.pdf. Accessed: 2018-2-23.

[39] EADS SPACE. Silex : More than one thousand successful optical links. http://www.spaceref.com/news/viewpr.html?pid=17298, June 2005. Accessed: 2018-1-26.

[40] Spaceflight. Pricing information. http://spaceflight.com/schedule-pricing/, 2018. Accessed: 2018-5-16.

[41] SPIE. Space-based optical communications presented at photonics west 2018. http://spie.org/conferences-and-exhibitions/photonics-west/2018-onsite-news/laser-communication?SSO=1. Accessed: 2018-5-16.

[42] Engineering Toolbox. Machine processing and tolerance grades. https://www.engineeringtoolbox.com/machine-processes-tolerance-grades-d1367.html, 2008. Accessed: 2018-4-26.

[43] Senay Unal. Creonic enables high-speed downlinks for aquia space's nanosatellites. https://www.creonic.com/en/news/creonic-dvb-s2-nanosatellite/, 2015. Accessed: 2018-5-15.

[44] Tethers Unlimited. Swift-slx. http://www.tethers.com/SpecSheets/, 2017. Accessed: 2018-5-16.

[45] Hyosang Yoon. Pointing system performance analysis for optical inter-satellite communication on cubesats, 2017.

[46] Warren C. Young. *Roark's Formulas for Stress and Strain.* McGraw-Hill, 2002.